L-Band Radiometry of Alpine Seasonal Snow Cover: 4 Years at the Davos-Laret Remote Sensing Field Laboratory

Reza Naderpour, Mike Schwank, Derek Houtz, and Christian Mätzler

***Abstract*—This study reports on four consecutive winter campaigns (2016–2020) at the "Davos-Laret Remote Sensing Field Laboratory" in the Swiss Alps to gain insight into the L-band microwave emission of ground covered with seasonal snow. Close-range L-band Brightness temperatures $T_{\mathrm{B}}^{p,\phi}(\theta)$ were measured over the site scanning different observation nadir angles θ and azimuth angles ϕ at horizontal and vertical polarization $p = \{\mathrm{H,V}\}$. State parameters (SPs) of the snowpack (e.g., height, density, and snow water equivalent) and the subnivean soil (permittivity, temperature) were measured quasi-simultaneously using in-situ sensors and sampling, as well as meteorological data. In each campaign, $T_{\mathrm{B}}^{p,\phi}(\theta)$ were measured over a "natural area" and a "reflector area" with a metal mesh reflector laid on the ground before snow accumulation. The radiometer measurements over "reflector area" allowed to retrieve the time-series of Snow liquid Water-content W_{S} and Snow liquid Water-Column WC_{S}, which are employed as "derived measurements" to support interpretation of $T_{\mathrm{B}}^{p,\phi}(\theta)$ measured over "natural areas" during different winter phases. The detailed approach for the estimation of W_{S} and WC_{S} using L-band radiometer data is presented. The data and analyses in this article address the following major points: 1) determination of the characteristic features of measured $T_{\mathrm{B}}^{p,\phi}(\theta)$ during different periods in each of the four winter campaigns; 2) effects of dry and wet snow precipitation on L-band radiometer data compared to corresponding simulations; 3) effect of removal and compression of the snowpack on $T_{\mathrm{B}}^{p,\phi}(\theta)$; 4) effects of spatial heterogeneity on brightness temperatures. Finally, the study is concluded with recommendations relevant for future close-range remote sensing campaigns.**

***Index Terms*—Alpine snow, Davos-Laret, ground permittivity, L-band radiometry, remote sensing of cryosphere, snow density, snow liquid water.**

I. Introduction

MICROWAVE radiometry was first performed on controlled and characterized snow samples to support the development and validation of emission models [1], [2], [3], [4]. Gradually, longer measurement campaigns were carried out to study the effects of temporal variations of snow cover and subnivean ground states on microwave emission. For example, long-term radiometry in the frequency range 5–100 GHz was performed in Weissfluhjoch (at 2550 m.a.s.l. near Davos, Switzerland) to study microwave signatures of snow under various conditions and to develop algorithms for snow-type classification, snow- mapping, and snow liquid water-content detection [5], [6]. Another example is four sessions of active- and passive close-range remote sensing (RS) together with a detailed characterization of snow cover reported in [1] and [2]. Each session lasted between one to three days and the purpose of the study was the exploration of active and passive microwave responses to snow parameters, such as wetness.

In the 1980s and 1990s, a lot of research has been invested in low-frequency passive RS at the L-band (1–2 GHz), including the development of corresponding microwave radiometers (RMs) and radiative transfer models, development of retrieval methods to estimate geophysical parameters based on L-band brightness temperatures, and the conduction of dedicated RS experiments. Most of these activities were aimed at gaining information about soil moisture, vegetation properties, and ground freeze/thaw. Notable examples of early RM-system developments include the National Aeronautics and Space Administration's (NASAs) PushBroom Microwave Radiometer (PBMR) [7], and the Electronically Scanned Thinned Array Radiometer (ESTAR) [8]. In connection with early microwave RS campaigns in support of model development and validation, the long series of Radiobrightness and Energy Balance Experiments [9], [10], [11], [12], [13], [14], [15] was conducted. Results of the mentioned activities culminated in the famous book series "Microwave Remote Sensing—Active and Passive" [16], [17], [18], which is still considered as reference literature in the field of microwave RS. Furthermore, the entirety of these early works laid the ground for later spaceborne microwave missions aiming to estimate soil moisture at large spatial scales.

Manuscript received 3 February 2022; revised 1 June 2022; accepted 28 July 2022. Date of publication 1 August 2022; date of current version 28 September 2022. This work was supported in part by the Swiss National Science Foundation under Grant 200021L_156111/1 (project MicroVegSnow) and Grant 200020L_182049 (project APRESS), in part by the European Space Agency (ESA) within the framework of the SMOS "Expert Support Laboratory" under Grant 4000113119, and in part by the SnowLab-NG Project under Grant 4000130865/20/NL/FF/AN. *(Corresponding author: Mike Schwank.)*

Reza Naderpour is with the Swiss Federal Institute for Forest, Snow, and Landscape Research, CH-8903 Birmensdorf, Switzerland (e-mail: reza.naderpour@wsl.ch).

Derek Houtz is with the Swiss Federal Institute for Forest, Snow, and Landscape Research, CH-8903 Birmensdorf, Switzerland, and also with TerraRad Tech AG, CH-8047 Zürich, Switzerland (e-mail: derek.houtz@wsl.ch).

Mike Schwank is with the Swiss Federal Institute for Forest, Snow, and Landscape Research, CH-8903 Birmensdorf, Switzerland, and also with the GAMMA Remote Sensing Research and Consulting AG, 3073 Gümligen, Switzerland (e-mail: mike.schwank@wsl.ch).

Christian Mätzler is with the GAMMA Remote Sensing Research and Consulting AG, 3073 Gümligen, Switzerland (e-mail: christian.matzler@iap.unibe.ch).

Digital Object Identifier 10.1109/JSTARS.2022.3195614

Examples of such current operational missions are the European Space Agency's (ESAs) Soil Moisture and Ocean Salinity (SMOS) [19] and the NASAs Soil Moisture Active Passive (SMAP) [20].

However, the topic of L-band radiometry in application to snow-covered areas did not receive momentum until the 2000s. This was mainly because of the small magnitude of the interaction between L-band radiation and dry snow, resulting in a very large penetration depth (>100 m [5], [21]). In consequence, RS researchers concentrated on higher frequencies where interaction with snow is significantly stronger, and the scientific consensus established that L-band radiometry could not provide information on snow cover properties. This narrative was challenged with the development of the L-band Specific Microwave Emission Model of Layered Snow (LS-MEMLS) in 2014 [22]. LS-MEMLS simulations showed that, despite the contemporary understanding that dry snow is "invisible" at L-band, it is merely "transparent", and thus, it influences Brightness temperature $T_{\mathrm{B}}^{p}(\theta)$ at different observation angles θ relative to nadir at horizontal and vertical polarization $p = \{\mathrm{H,V}\}$ via impedance matching and refraction.

With the launch of the L-band missions SMOS [19] and SMAP [20], long-term L-band radiometry of the Cryosphere became more interesting in the scientific community and led to the theoretical study [23] proposing an approach to retrieve Snow density and Ground permittivity $(\rho_{\mathrm{S}}, \epsilon_{\mathrm{G}})$ from L-band $T_{\mathrm{B}}^{p}(\theta)$. Such developments laid ground for long-term tower-based L-band radiometry in multiple climate regions including the Finnish Meteorological Institute's Arctic Research Center (FMI-ARC) since 2009 [24], the Tibetan plateau since 2016 [25], and in Poland since 2017 [26].

The measurements at FMI-ARC experimentally confirmed the model prediction that dry snow affects $T_{\mathrm{B}}^{p}(\theta)$ and that $(\rho_{\mathrm{S}}, \epsilon_{\mathrm{G}})$ can be retrieved from L-band RM $T_{\mathrm{B}}^{p}(\theta)$ data. Accordingly, in Autumn 2016, the Davos-Laret Remote Sensing Field Laboratory [27] was established for the tower-based RS of seasonal snow cover. The Davos-Laret site was complementary to the other sites with long-term microwave RS in terms of climate and instrumentations; it was an alpine site at an altitude of 1420 m.a.s.l. and it included multifrequency active and passive RS instruments. In addition, the Davos-Laret site included artificially prepared areas (e.g., a reflective wire grid) to study specific radiation transport mechanisms (e.g., absorption of the snow) from the start.

The first winter Campaign (C1) was conducted in 2016/2017 and resulted in increased understanding of the effect of geophysical and instrumental noise on two-parameter retrievals $(\rho_{\mathrm{S}}, \epsilon_{\mathrm{G}})$ [28], and the retrieval of Snow liquid Water-content W_{S} [29]. Additionally, sensitivities of L-band $T_{\mathrm{B}}^{p}(\theta)$ and derived retrievals $(\rho_{\mathrm{S}}, \epsilon_{\mathrm{G}})$ to various snow- and ground-SPs were analyzed. The examples include the effect of W_{S} and its distribution pattern across the snowpack [27] and the effect of subnivean layer permittivity and roughness [23]. Some of the synthetic sensitivity analysis previously available in the literature lacked the experimental pairs simply due to lack of observations. This included for instance the observations over unfrozen ground covered with snow.

We present results from four consecutive winter Campaigns, C1 to C4, for winter seasons between 2016 to 2020, which provide experimental validation to some of the previously theoretically inspected cases. Accordingly, first, we provide an overview of the measurements performed during C1 to C4. To do so, a description of the site together with its setup schematics for different campaigns is given in Section II. Section III-A provides the introduction to the employed L-band RMs and the methods for the computation of calibrated Brightness temperatures $T_{\mathrm{B}}^{p}(\theta)$ and for quantification of non-thermal Radio Frequency Interference (RFI). Sections III-B and III-C focus on the in-situ soil, snow, and on-site meteorological measurements. Considering the large volume and variety of data, Section IV provides an overview of the measurements, which are available through this publication [30]. To help better understand the L-band emission from natural ground covered with snow, we use Snow liquid Water-content W_{S} and thereon based Snow liquid Water-content WC_{S}. The latter are considered as "derived measurements" because they are retrieved from L-band brightness temperature measured over FootPrint (FP) areas with a reflector beneath the snowpack. This approach was first applied in [29] using brightness temperatures measured during C1 at the Davos-Laret site. Later studies [31], [32], [33] utilized conceptually similar retrieval methods to estimate snow melt over the Greenland ice sheet. However, due to the central importance of W_{S} and WC_{S} derived for all four campaigns, their underlying retrieval approach is described in Sections IV. Section V consists of graphic overviews of the core measurements with a brief description of the main features of each campaign. Further information and measurements are included in the data package linked to [30].

Furthermore, four more detailed example analyses are provided to study the effect of precipitation (Section VII), snow removal and compression (Section VIII), spatial heterogeneities over the site (Section IX), and the intercomparison of angular patterns of $T_{\mathrm{B}}^{p}(\theta)$ for all campaigns (Section VI). It is noteworthy that, in addition to their scientific value, these analyses are examples of how one can employ the data collected during these campaigns for various scientific investigations.

II. Site Description

The measurements reported and used in this article were conducted at the Davos-Laret Remote Sensing Field Laboratory [27], henceforth called "Davos-Laret RS site" or "site." Situated at the Laret valley ($46°50'43''$N, $9°52'19''$E) at an altitude of 1420 m a.s.l., this site was established in autumn 2016 for long-term close-range active and passive microwave RS of alpine snow. The site extends over $\sim 50 \times 50$ m; it is relatively flat with small undulations of less than a meter height surrounding all but the northeastern side. Fig. 1 shows an aerial image of the site highlighting its position with respect to the neighboring Lake-Schwarz, residential area, and the forested regions. The location of the microwave RM tower and multiple sets of FP areas over the site during the winter Campaigns 2016/2017 (C1), 2017/2018 (C2), and 2018/2019 (C3) are depicted in Fig. 1. The site is normally covered with grass, which was cut at

Fig. 1. Overview photo of the Davos-Laret RS site with indicated RM tower and FP observed during the winter Campaigns C1 (2016/2017), C2 (2017/2018), and C3 (2018/2019). The layouts of all four campaigns, including C4 (2019/2020), are outlined in detail in Fig. 2.

TABLE I
INFORMATION ON THE POSITIONS OF THE SOIL IN-SITU SENSORS DEPLOYED ALONG TRANSECTS (T#) SHOWN IN FIG. 2 DURING THE CAMPAIGNS C1–C4 WITH INCREASING DISTANCE FROM THE RM TOWER ALONG THE T#, IDS OF SMT-100 AND 5TE FORK SENSORS ARE INDICATED AS S# AND F#, RESPECTIVELY

Campaign # (C#)	Transect (T#)	Sensor IDs
C1	T1	S2, F2, S3, F3, S4, S5, S6, S7
	T2	S8, F4, S9, F5, Sa, Sc, Sd, Se
	in snow	F1, S0, S1
C2	T1	Sf, Si, Sh, Sg, Sj, Sd, Se, Sc
	T2	S8, Sb, F5, S9, Sa, F4, S6
	T3	S0, S1, F1, F2, S3, F3, S4, S5
C3	T1	S0, S1, S2, F1, F2, S3, F3, S4, S5
	T2	S6, F4, S7, F5, S8, S9
C4	T1	(S5, S0), (S8, S1), (S9, S2), (Sa, S3), (Sb, S4)
	T2	Si, Sh, Sg, Sf, Se, Sd, Sc, S6, S7
	T3	F1, F4, F5, Sj
	small reflector	F2, F3

the end of the autumn each year in preparation for the winter measurement campaigns. Depending on the weather conditions, ground freeze/thaw status, and the duration between the last grass harvest and snow appearance, the grass could grow before the onset of snow. Fig. 2(a) illustrates the schematics of the site during the first three Campaigns (C1–C3). The red dash-dotted lines show the four observation directions at respective azimuth angles $\phi = \{35^\circ, 90^\circ, 145^\circ, 200^\circ\}$ labeled with red boxes. The dashed ellipsoids indicate the projected -9 dB FPs of the L-band RMs' Picket-horn antenna [34] pointing at the range $30^\circ \leq \theta \leq 60^\circ$ of angles θ relative to nadir. A complete scan consisting of the four azimuth angels ϕ and seven nadir angles $\theta = \{30^\circ, 35^\circ, 40^\circ, 45^\circ, 50^\circ, 55^\circ, 60^\circ\}$ was performed hourly. During C1 to C3, a metal-mesh reflector (gray-shaded trapezoidal area) was placed on the ground along $\phi = 145^\circ$ for FPs corresponding to $30^\circ \leq \theta \leq 60^\circ$. As demonstrated in [29], the "reflector area" allows for the measurement of snowpack's self-emission in presence of snow liquid water content. As is illustrated in Fig. 2(b), arrangements of FPs observed during the fourth Campaign C4 were different with respect to C1–C3. During C4 in winter 2019/2020, the ESA's Wide-Band SCATterometer (WBSCAT) [35], [36], [37] was used in addition to the L-band RM to perform simultaneous active (L- to Ka-band) and passive (L-band) close-range microwave measurements of alpine snow cover [38]. In C4, a double-layer artificial area was designed and prepared. The first layer was composed of charcoal mixed with soil and on top of it was a surface layer of fine-grained sand. This "charcoal-sand area", shown in white in Fig. 2(b), was designed such that both WBSCAT and the L-band RM pointing at $\phi = 75^\circ$ and $\theta = \{35^\circ, 40^\circ, 45^\circ\}$ could observe it. The reason for this experimental setup was to decrease the backscattering from the Snow–Ground (S-G) interface and, thus, to study the backscattering of the snow with reduced blending of backscatter originating from the S-G interface. Additionally, a small reflector with fine mesh-grid cells ($\sim$1 mm) was placed underneath WBSCAT along its boresight to allow for measurement of snow backscatter without any influence from the underlying ground. The photo at the center-right of Fig. 2(b) shows the "charcoal-sand area" and the "small reflector area" in C4. As explained in the following, in-situ sensors were used to monitor properties of these artificial FP areas.

Several Transects (T) are shown in Fig. 2 to depict the location of deployed in-situ sensors measuring dielectric permittivity ϵ_{G} (real part) and temperature T_{G} of the Ground. Two types of in-situ sensors were buried $\sim$ 5 cm below the soil surface: 1) SMT-100 and 2) 5TE fork sensors depicted in Fig. 2 with green circles and black crosses, respectively. A green circle with a black cross is used to indicate where an SMT-100 and a 5TE sensor were placed at the same location. Examples for this case are Transects 2 and 3 during Campaign 2 indicated with T2(C2) and T3(C2), respectively. In Fig. 2(b), green dots encircled by green circles are used to indicate the pairs of SMT-100 sensors over T1(C4) deployed at $\sim$15 cm and $\sim$3 cm below the surface to measure the charcoal-soil mix and sand layer properties, respectively. In addition to the sensors buried in the ground, during C1, sensors were installed on a wooden stick [orange circle indicated in Fig. 2(a)] to measure permittivity and temperature of the snow. The respective 5TE and the two SMT-100 sensors were installed 10-cm, and 15-, 50-cm above ground. Data measured by these three sensors are not reported here but included in the data package made available in [30].

Table I contains the sensor IDs for each of the Transects (T) in each Campaign (C) ordered based on increasing distance from the RM tower. In Table I, the IDs given for SMT-100 and 5TE Fork sensors begin with letters "S" and "F", respectively, followed by the sensors' identifying letter or number. Further information about the deployed in-situ sensors and their measurements is provided in Section III-B. It is noteworthy that in this article, we only show permittivity ϵ_{G} measured by SMT-100 sensors. This is because SMT-100 directly output ϵ_{G} while 5TE sensors include an internal transformation to output soil moisture.

The neighboring SCATerometer (SCAT) tower, depicted in Fig. 2, hosted the SCATterometers SnowSCAT [39] during C1, C2, and C3 and WBSCAT [40] during C3 and C4 [38]. The emitted signals from these scatterometers could cause RFI disturbing the brightness temperatures measured by the RM. Furthermore, the towers were made of metal parts and thus could reflect the RFI signal into the RMs' antenna whenever the RM would point

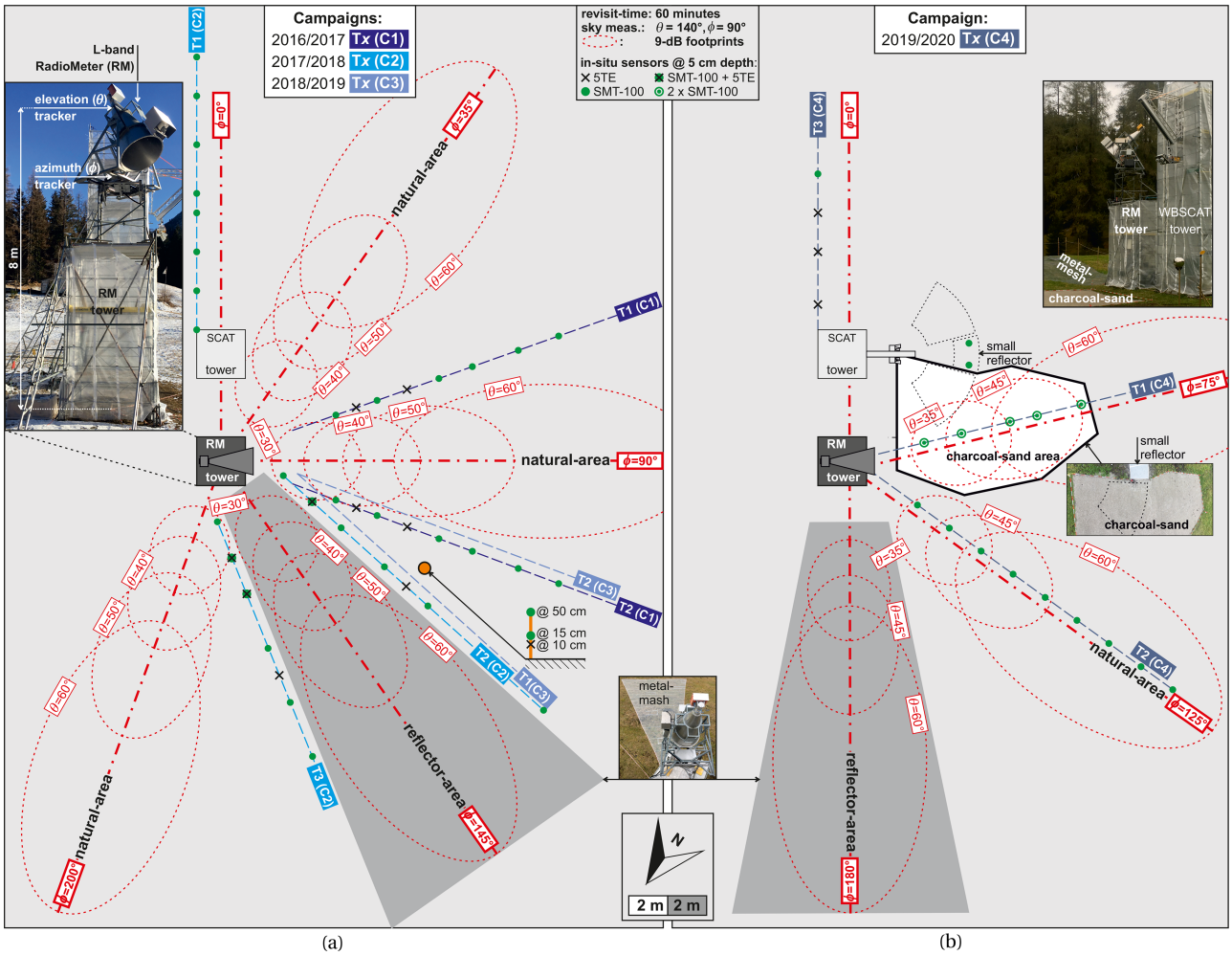

Fig. 2. (a) Schematics of the experimental setups implemented during the three Campaigns C1, C2, and C3. (b) Setup used in C4.

toward the towers. As a result, $T_{\mathrm{B}}^{p,\phi}(\theta)$ measured at polarization $p = \{\mathrm{H,V}\}$ along the azimuth angle $\phi = 35°$ are nonideal. The FP areas along $\phi = 200°$ were outside the formally defined and fenced site. Therefore, measured L-band $T_{\mathrm{B}}^{p,200°}(\theta)$ are considered with care, and only used for specific case studies and to investigate the effect of spatial heterogeneities on the measured brightness temperatures.

III. Experimental Setup

In addition to L-band radiometry, meteorological as well as in-situ snow and soil measurements were carried out during each campaign. Here, we provide a description of each of the experimental setup elements.

A. L-Band RMs

Throughout the four winter campaigns, two different microwave RMs were used to measure Brightness temperatures $T_{\mathrm{B}}^{p,ch}$ at horizontal and vertical polarization $p = \{\mathrm{H,V}\}$ within two 11-MHz channels $ch = \{1,2\}$ in the protected part (1.400–1.427 GHz) of the L-band (1–2 GHz). In the first two Campaigns C1 (winter 2016/2017) and C2 (winter 2017/2018), it was the ETH L-BAnd RAdiometer (ELBARA-II), in the subsequent Campaigns C3 (winter 2018/2019) and C4 (winter 2019/2020), it was a modified JÜlich L-Band RAdiometer (JÜLBARA) nicknamed OMRA for Office Made RAdiomter.

The Radio Frequency (RF) frontend implemented in ELBARA-II and OMRA is literally the same resulting in similar performances in terms of accuracy ($\sim \pm 1$K) and sensitivity ($\sim$0.1 K). Both RMs split the antenna signals in two 11-MHz frequency channels $ch = \{1,2\}$ to enable detection of RFI in the frequency domain. Furthermore, the same Picket-horn antenna [34] connected with low-loss coaxial Feed Cables (FC) was used. The aperture size of the antenna was $\sim$1.4 m and its Half-Power (-3 dB) Full Beamwidth (HPFB) was $\sim 12°$. Accordingly, the directional sensitivity of the shared Picket-horn antenna is strongly concentrated around its boreside, and sensitivities of side- and back lobes are less than ~ -14.3 dB relative to the boreside sensitivity. The exact dimensions and the experimental characterization of the Picket-horn directivity is shown in [41].

As shown at the top left in Fig. 2(a), ELBARA-II or OMRA was mounted on a scaffold equipped with an automatic elevation-azimuth tracker. This tracking system, controlled by the instrument computer of the respective RM, allowed for regular scanning of the site along multiple nadir and azimuth angles θ and ϕ, respectively (Fig. 2). Installation heights of the RMs were consistent in all campaigns, such that the phase center

of the Picket-horn antenna was ∼8 m above ground. However, ELBARA-II and OMRA differ in 1) the internal calibration sources; 2) the temperature stabilization; 3) the data acquisition and the instrument computer:

1) ELBARA-II: ELBARA-II [41] used in C1 and C2 is a temperature stabilized L-band RM equipped with an internal matched resistive noise source of known physical and equivalent noise temperature T_{R}, and with an Active Cold Source (ACS). Noise temperature T_{ACS} of the ACS is determined by regular measurements toward the sky ($\phi = 90^\circ$ and $\theta = 140^\circ$) whose L-band brightness temperature T_{sky} can be computed using existing models, for instance [42]. Calibrated $T_{\mathrm{B}}^{p,ch}$ are achieved from ELBARA-IIs raw data (voltages) measured toward FPs, and T_{R} and T_{ACS} associated with corresponding voltage readings. Here, we refrain from further explanation on the calibration of ELBARA-II, as this is already described in [27], for instance. In [43], it is shown that absolute uncertainty of RFI-free ELBARA-II measurements $T_{\mathrm{B}}^{p,ch}$ is $\sim\pm 1$ K for the range of brightness temperatures expected from observed FPs.

2) OMRA: OMRA used in C3 and C4 is developed from a JÜLBARA [44] upgraded with a "Raspberry Pi" instrument computer to have digital data acquisition and interfaces to control the automatic elevation-azimuth tracker. JÜLBARA and, therefore, also OMRA took over the RF frontend from ELBARA-0 [45]. Similar to ELBARA-II, the RF Assembly (RFA) in OMRA (= JÜLBARAs RFA) is installed on a metal plate with high thermal inertia to minimize thermal gradients. However, unlike to ELBARA-II, the RFA in OMRA is not accurately temperature stabilized. Instead, the entire JÜLBARA RF frontend was enclosed in a weatherproof housing equipped with heating elements that switch ON automatically when internal temperature drops below ∼20 °C. This means that OMRAs RFA temperature variability in response to ambient temperature is at least limited. Without the additional enclosure, operation of the original JÜLBARA RF frontend under harsh environmental conditions would have been a problem. For instance, the measure taken prevents RFA temperature from dropping below the dew point and, therefore, the formation of condensation. Furthermore, OMRA is equipped with matched resistive cold and hot noise sources (no Active Cold Source (ACS) as in ELBARA-II). Physical temperatures of the resistive cold and hot noise sources are stabilized to $T_{\mathrm{cold}} \approx 4\,^\circ\mathrm{C}$ and $T_{\mathrm{hot}} \approx 44\,^\circ\mathrm{C}$, respectively. The accurate match of both resistive sources with the 50-Ω impedance of the RF frontend input ensures that physical temperatures T_{cold} and T_{hot} correspond with respective noise temperatures.

It is obvious that the mentioned technical differences between OMRA and the more recent ELBARA-II require different methods to achieve calibrated Brightness temperatures $T_{\mathrm{B}}^{p,ch}$ from the raw data (voltages) of the two RMs. Since the calibration method used with OMRA was newly developed, it is briefly outlined.

The original method to obtain calibrated $T_{\mathrm{B}}^{p,ch}$ from OMRA is the same as the one employed with ELBARA-0 [45], detailed in [46], [47], and [48], and further applied in [49]. That approach uses T_{cold} and T_{hot}, which are relatively close in magnitude compared to ELBARA-II, and thus relies on extrapolation to compute $T_{\mathrm{B}}^{p,ch}$. Such an extrapolation and lack of characterization of temperature-dependent performance of the RFA can lead to inaccurate $T_{\mathrm{B}}^{p,ch}$. In this work, we introduce an alternative approach that improves the calibration of $T_{\mathrm{B}}^{p,ch}$.

The first calibration step uses sky measurements performed at $\phi = 90^\circ$ and $\theta = 140^\circ$. From each undistorted sky measurement *j*, four data-pairs $(U_{\mathrm{sky},j}^{p,ch}, T_{\mathrm{sky},j})$ are created corresponding to $p = \{\mathrm{H,V}\}$ and $ch = \{1,2\}$. Downwelling sky radiance $T_{\mathrm{sky},j}^{*}$ at the antenna aperture (*) at recorded $T_{\mathrm{air},j}$, $\theta = 140^\circ$ and the site altitude 1420 m a.s.l. is simulated with the model presented in [42]. Subsequently, thermal noise emitted by each of the two FC, connecting the horizontal and the vertical ports of the antenna, is added to achieve $T_{\mathrm{sky},j}$ at the corresponding OMRA input port

$$T_{\mathrm{sky},j} = T_{\mathrm{sky},j}^{*} + (1 - t_{\mathrm{FC}})\cdot(T_{\mathrm{FC},j} - T_{\mathrm{sky},j}^{*}). \tag{1}$$

Transmissivity $t_{\mathrm{FC}} = 10^{-L_{\mathrm{FC}}/10}$ of each FC is related to its transmission loss specified as $L_{\mathrm{FC}} = 0.3$ dB. FCs physical temperature is represented by measured air temperature $T_{\mathrm{FC}} = T_{\mathrm{air},j}$.

In addition to the now available data $(U_{\mathrm{sky},j}^{p,ch}, T_{\mathrm{sky},j})$, there exist further 2×2 data-pairs $(U_{\mathrm{cold},j}^{ch}, T_{\mathrm{cold},j})$ and $(U_{\mathrm{hot},j}^{ch}, T_{\mathrm{hot},j})$ from measuring the cold and hot resistive sources (at $ch = \{1,2\}$) kept at the physical temperatures $T_{\mathrm{cold}} = 4\,^\circ\mathrm{C} \approx T_{\mathrm{cold},j}$ and $T_{\mathrm{hot}} = 44\,^\circ\mathrm{C} \approx T_{\mathrm{hot},j}$ equivalent to their respective noise temperatures.

The linear model below is adapted to the data-pairs $(U_{\mathrm{sky},j}^{p,ch}, T_{\mathrm{sky},j})$ and $(U_{\mathrm{cold},j}^{p,ch}, T_{\mathrm{cold},j})$, $(U_{\mathrm{hot},j}^{p,ch}, T_{\mathrm{hot},j})$ resulting in the optimal fit-parameters $A_j^{p,ch}$ and $B_j^{p,ch}$ for each sky measurement *j*

$$T^{p,ch}(U^{p,ch}) = A_j^{p,ch} + B_j^{p,ch}\cdot U^{p,ch}. \tag{2}$$

The values of these 2×4 fit parameters change with ambient temperature because OMRAs RF frontend is not accurately temperature stabilized. Instead, it is built from JÜLBARAs RF frontend enclosed in an additional housing, as discussed above. However, for each measurement *j*, performed at $T_{\mathrm{air},j}$, temperature $T_{\mathrm{RFA},j}$ is measured at the thermally inert metal plate carrying temperature-sensitive RFA components (amplifiers and attenuators, for instance). This ensures that temperatures of these components are very similar and well represented by measured $T_{\mathrm{RFA},j}$. With these considerations, it is clear that the available 2×4 datasets $(T_{\mathrm{RFA},j}, A_j^{p,ch})$ and $(T_{\mathrm{RFA},j}, B_j^{p,ch})$ specify OMRAs residual noise and gain, respectively, at recorded $T_{\mathrm{RFA},j}$ and $p = \{\mathrm{H,V}\}$ and $ch = \{1,2\}$.

The following second-order polynomials, fit to each of the datasets $(T_{\mathrm{RFA},j}, A_j^{p,ch})$ and $(T_{\mathrm{RFA},j}, B_j^{p,ch})$ derived from sky measurements, yield the 2×4 models that represent OMRAs residual noise and gain at temperature T_{RFA} at $p = \{\mathrm{H,V}\}$ and $ch = \{1,2\}$

$$A^{p,ch}(T_{\mathrm{RFA}}) = a_1^{p,ch} + a_2^{p,ch}\cdot T_{\mathrm{RFA}} + a_3^{p,ch}\cdot T_{\mathrm{RFA}}^2 \tag{3}$$

$$B^{p,ch}(T_{\mathrm{RFA}}) = b_1^{p,ch} + b_2^{p,ch}\cdot T_{\mathrm{RFA}} + b_3^{p,ch}\cdot T_{\mathrm{RFA}}^2. \tag{4}$$

With the models $A^{p,ch}(T_{\mathrm{RFA}})$ and $B^{p,ch}(T_{\mathrm{RFA}})$, noise temperatures at the input ports (*) of OMRA are computed as:

$$T_{\mathrm{B}}^{*p,ch}(U_{\mathrm{FP}}^{p,ch}, T_{\mathrm{RFA}}) = A^{p,ch}(T_{\mathrm{RFA}}) + B^{p,ch}(T_{\mathrm{RFA}}) \cdot U_{\mathrm{FP}}^{p,ch} \tag{5}$$

Voltages $U_{\mathrm{FP}}^{p,ch}$ are raw data measured when OMRA is pointing toward the FP of interest and RFA temperature T_{RFA} is measured simultaneously.

Finally, in analogy to (1), calibrated Brightness temperatures $T_{\mathrm{B}}^{p,ch}$ at the antenna aperture (also called "antenna temperature") is computed from $T_{\mathrm{B}}^{*p,ch}$ at the OMRAs inputs by adding the thermal noise of the FC

$$T_{\mathrm{B}}^{p,ch}(U_{\mathrm{FP}}^{p,ch}, T_{\mathrm{RFA}}) = \frac{T_{\mathrm{B}}^{*p,ch} - T_{\mathrm{FC}}(1 - t_{\mathrm{FC}})}{t_{\mathrm{FC}}} \tag{6}$$

As above, the physical temperature of the FC is considered as $T_{\mathrm{FC}} = T_{\mathrm{air}}$.

From (3), (4), and (5) it is clear that the accuracy of OMRAs calibration depends on the uncertainties $\Delta A^{p,ch}$ and $\Delta B^{p,ch}$. The latter are estimated as the median (med) of the absolute values of associated *j* residuals (res) $Ares_j^{p,ch}$ and $Bres_j^{p,ch}$ for *p*={H,V} and *ch*={1,2}

$$\begin{aligned} \Delta A^{p,ch} &= \mathrm{med}(Ares_j^{p,ch}) \text{ with } Ares_j^{p,ch} \\ &= |A^{p,ch}(T_{\mathrm{RFA},j} - A_j^{p,ch})| \end{aligned} \tag{7}$$

$$\begin{aligned} \Delta B^{p,ch} &= \mathrm{med}(Bres_j^{p,ch}) \text{ with } Bres_j^{p,ch} \\ &= |B^{p,ch}(T_{\mathrm{RFA},j} - B_j^{p,ch})|. \end{aligned} \tag{8}$$

The result is $\Delta A^{p,ch} \approx 2$ K and $\Delta B^{p,ch} \approx 0.5$ KV^{-1} leading to uncertainties $\Delta T_{\mathrm{B}}^{p,ch} \approx 2$ K in OMRAs calibrated Brightness temperatures $T_{\mathrm{B}}^{*p,ch}$ at the input ports computed with (5)

$$\Delta T_{\mathrm{B}}^{p,ch} = \sqrt{\Delta A^{p,ch\,2} + U_{\mathrm{FP}}^{p,ch} \cdot \Delta B^{p,ch}}. \tag{9}$$

3) RFI: As described above, raw data (voltages) are used to compute the calibrated $T_{\mathrm{B}}^{p,ch}$ for both ELBARA-II and OMRA. Measurement at two frequency channels *ch*={1,2} within the protected part of the L-band enables detection of narrow-band RFI. A measurement, which is distorted by narrow-band RFI, is identified when channel difference $\Delta T_{\mathrm{B}}^{p,ch} \equiv |T_{\mathrm{B}}^{p,1} - T_{\mathrm{B}}^{p,2}|$ exceeds a certain threshold. For ELBARA-II and OMRA, measurements exhibiting $\Delta T_{\mathrm{B}}^{p,ch} \geq 1.5$ K and $\Delta T_{\mathrm{B}}^{p,ch} \geq 5$ K, respectively, are excluded from the data shown here but are still included in the data package [30]. This data include $\Delta T_{\mathrm{B}}^{p,ch}$ values.

An additional method used here to identify non-thermal RFI is the Probability Density Function method (PDF-method) developed and described in [27]. Its concept consists of the comparison between the PDF of raw-data voltage samples measured (at the sampling frequency of 800 Hz and a 3-s integration time) and the Gaussian distribution expected for samples associated with undisturbed, purely thermal microwave radiation. Compared to conventional "normality" tests (kurtosis and skewness [50]), the "PDF-method" offers significant advantages: First, it is more responsive to certain types of time-domain RFI. Second, it allows quantifying the extent $\Delta T_{\mathrm{B,non-thermal}}^{p}$ to which $T_{\mathrm{B}}^{p,ch}$ is distorted by non-thermal radiance. In the data shown here, the measurements with $\Delta T_{\mathrm{B,non-thermal}}^{p} \geq 1.5$ K are omitted.

B. In-Situ Soil and Snow Measurements

As explained in Section II (Table I and Fig. 2) in-situ SMT-100 and 5TE fork sensors were used in each campaign. The SMT-100 sensors [51] measure temperature and real dielectric permittivity at $f \approx 100$ MHz. The permittivity is used as a proxy to also output volumetric water-content. Additionally, five 5TE sensors [52], [53] were used to measure temperature, volumetric soil water-content, and electrical conductivity. The sensor measurements were conducted using a DT80 data logger every 5 min. There exist some data gaps in the recorded data due to technical problems with the data logger during some campaigns. More information is provided in Section V.

Furthermore, weekly manual snow characterization was carried out on the site to keep track of snow profile variations. In the case of heavy snow falls, snow characterization was conducted immediately afterward to capture resulting abrupt changes. Snow density ρ_{S} was measured with a 3-cm density cutter. Additionally, Snow Water Equivalent (SWE) and Snow temperature T_{S} were recorded next to Near Infra-Red (NIR) images of the profile's cross section. The latter helps identify snow layering and internal macrostructural features, which can be relevant in the analysis of L-band brightness temperatures. Photos taken by several webcams provide another useful source of information for the qualitative assessment of snowpack conditions. Time-lapse videos generated from these photos are part of the data package made available [30].

C. Automatic Weather Station

During the winter campaigns, several meteorological, snow, and ground parameters were recorded hourly by an on-site Automatic Weather Station (AWS). These parameters include air temperature T_{air} at 2 m, relative humidity, melted equivalent Precipitation *Prec.* (rain or snow), incoming and reflected shortwave radiation, Snow height h_{S} and Snow Surface temperature T_{SS}, wind speed and direction, as well as SWE. In this article, we report and use T_{air}, h_{S}, and *Prec.*, which are available throughout the four Campaigns. The AWS used during C1 and C2 did not include a snow balance. This AWS was upgraded for the following Campaigns C3 and C4. Accordingly, hourly AWS recordings of SWE were available only during C3 and C4. Nevertheless, SWE derived from weekly snow characterization is available for all four campaigns.

IV. Datasets

Table II provides a summary of important dates and main characteristics of all Campaigns C1 to C4. Most notably the length of campaigns increased from 109 days in C1 to 223 days in C4. However, C4 was the only campaign in which the measurements stretched in time from before snow cover to after complete melt. In C1 and C3, at least one snow-free period exists while C2 began and ended in presence of snow cover. Finally, it is noteworthy that both situations of unfrozen ($\epsilon_{\mathrm{G}} \gg 5$) and

TABLE II
OVERVIEW OF CAMPAIGN (C) CHARACTERISTICS

	C1 (2016/20017)	C2 (2017/2018)	C3 (2018/2019)	C4 (2019/2020)
C start	25.11.2016	16.11.2017	13.12.2018	01.10.2019
C end	14.03.2017	13.04.2018	23.05.2019	10.05.2020
C duration	109 days	145 days	162 days	223 days
snow cover start	03.01.2017	12.11.2017	N.A.	08.11.2019
snow cover end	30.03.2017	24.04.2018	19.05.2019	17.04.2020
ground condition	frozen	unfrozen	unfrozen	unfrozen
FP types	"natural area", "reflector area"	"natural area", "reflector area"	"natural area", "reflector area"	"natural area", "reflector area", "charcoal-sand area"

frozen ($\epsilon_{\mathrm{G}} \approx 5$) ground conditions [27] occurred within C1 to C4.

The presented data comprise six categories through all four campaigns. These are described below, with detailed explanations regarding the Snow liquid Water-content W_{S} retrieved from $T_{\mathrm{R}}^{p}(\theta)$ of the "Reflector area."

The first category is time-series of Brightness temperatures $T_{\mathrm{B}}^{p,\phi}(\theta)$ at polarization p={H,V} measured for multiple azimuth angles ϕ and nadir angles $\theta = \{30^{\circ}, 35^{\circ}, \ldots, 60^{\circ}\}$ in 5° steps (Fig. 2). We focus here on measurements along $\phi = 90^{\circ}$ for C1–C3 and $\phi = \{75^{\circ}, 125^{\circ}\}$ for C4. As mentioned in Section III-A3, RFI corrupted $T_{\mathrm{B}}^{p,\phi}(\theta)$ are filtered and excluded from the analysis. The second set is Precipitation (*Prec.*) measured as rain or melted snow. To qualitatively assess the wetness of the Precipitation, we distinguish between *Prec.* measured at $T_{\mathrm{air}} < 0\,^{\circ}\mathrm{C}$ and $T_{\mathrm{air}} \geq 0\,^{\circ}\mathrm{C}$. The third and fourth sets of data are recorded Snow height h_{S} and air temperature T_{air}. The fifth set is the in-situ measured Ground permittivity ϵ_{G} averaged over the sensors deployed on the corresponding Transects (T) during a Campaign (C) indicated in Fig. 2, with sensors IDs provided in Table I.

The sixth dataset is a time-series of volumetric liquid Water-content W_{S} of Snow, and Snow liquid Water-Column $WC_{\mathrm{S}} = W_{\mathrm{S}} \cdot h_{\mathrm{S}}$. As outlined in [29] W_{S} is retrieved from the multiangle, measurement-based brightness temperatures $T_{\mathrm{R}}^{p}(\theta)$ emitted by solely the Reflector area (R) and, therefore, understood as a "derived measurement." The latter help to better understand responses of L-band $T_{\mathrm{B}}^{p,\phi}(\theta)$ measured over "natural areas" to changing S-G conditions. The usefulness of the retrieved W_{S} to explore active RS signature's response to snow melt and wetness variations is demonstrated in [38]. In the following, we outline the procedure for obtaining W_{S} and explain the campaign-specific considerations:

As explained in Section II, the RM antenna was pointed toward the "reflector area" ($\phi = 145^{\circ}$ in C1–C3 and $\phi = 180^{\circ}$ in C4) to measure the snowpack's own emission at L-band. However, due to inevitable measurement nonidealities such as antenna's finite directivity, the RM would measure emission originating from both the artificially prepared "reflector area" and the surrounding "natural area" with no reflector laid on the ground before snow deposition. Therefore, the first step toward obtaining W_{S} is to compute and deduct the partial contribution of the surrounding "natural area" from the total recorded measurement. This leads to the emission $T_{\mathrm{R}}^{p}(\theta)$ exclusively from the snowpack over the "Reflector area." Therefore, one must compute the weighting-factors $\mu_{\mathrm{R}}^{p,\theta}$ to express $T_{\mathrm{B}}^{p,\phi_{\mathrm{R}}}(\theta)$ measured for ϕ_{R}, as the linear combination of $T_{\mathrm{B}}^{p,\phi_{\mathrm{N}}}(\theta)$ measured for ϕ_{N} and the sought $T_{\mathrm{R}}^{p}(\theta)$. Assuming the reflectivity of the metal mesh reflector placed on the ground as one [43], [54], this yields

$$T_{\mathrm{B}}^{p,\phi_{\mathrm{R}}}(\theta) = \mu_{\mathrm{R}}^{p,\theta} \cdot T_{\mathrm{R}}^{p}(\theta) + (1 - \mu_{\mathrm{R}}^{p,\theta}) \cdot T_{\mathrm{B}}^{p,\phi_{\mathrm{N}}}(\theta). \tag{10}$$

As sketched in Fig. 2(a), for C1–C3 the azimuth angle of the "Reflector area" was $\phi_{\mathrm{R}} = 145^{\circ}$ and the azimuth angle of the chosen "natural area" was $\phi_{\mathrm{N}} = 90^{\circ}$. For C4, the respective azimuth angles are $\phi_{\mathrm{R}} = 180^{\circ}$ and $\phi_{\mathrm{N}} = 125^{\circ}$, as shown in Fig. 2(b).

For snow-free or dry-snow conditions $T_{\mathrm{R}}^{p}(\theta)$ is assumed as the reflected downwelling sky radiance $T_{\mathrm{sky}}(\theta)$ simulated with the model presented in [42]. Accordingly, $\mu_{\mathrm{R}}^{p,\theta}$ can be computed from (10) using $T_{\mathrm{B}}^{p,\phi_{\mathrm{R}}}(\theta)$ and $T_{\mathrm{B}}^{p,\phi_{\mathrm{N}}}(\theta)$ measured during "μ-calibration periods" defined by snow-free or dry-snow conditions.

For C1 and $\theta = \{40^{\circ}, 45^{\circ}, 50^{\circ}, 55^{\circ}, 60^{\circ}\}$, the "$\mu$-calibration period" was 20 December 2016 00:00 – 2 January 2017 00:00, before onset of snow. During this period, no RFI-free measurements were available for $\theta = \{30^{\circ}, 35^{\circ}\}$. Accordingly, for $\theta = 30^{\circ}$ the "μ–calibration period" was selected as 14 January 2017 00:00 – 15 January 2017 00:00, during the "mid-winter period" (Fig. 3) when the snowpack of height $h_{\mathrm{S}} \approx 35\ \mathrm{cm}$ was definitively dry with persistent $T_{\mathrm{air}} < -5\ ^{\circ}\mathrm{C}$. Likewise, for $\theta = 35^{\circ}$, the "μ-calibration period" was 5 January 2017 00:00 – 6 January 2017 00:00, during the "mid-winter period" with $h_{\mathrm{S}} = 50\ \mathrm{cm}$ and $T_{\mathrm{air}} < -5\ ^{\circ}\mathrm{C}$. For C2 and $\theta = \{35^{\circ}, 40^{\circ}, 45^{\circ}, 50^{\circ}, 55^{\circ}, 60^{\circ}\}$ the "μ-calibration period" was selected as 30 November 2017 00:00 – 2 December 2017 00:00, during the "early-winter period" (Fig. 4) with $h_{\mathrm{S}} \approx 30\ \mathrm{cm}$ and persistent $T_{\mathrm{air}} < -5\ ^{\circ}\mathrm{C}$ ensuring the snowpack was dry. For $\theta = 30^{\circ}$, no RFI-free RM measurements were available during an adequate period; therefore, $\mu_{\mathrm{R}}^{p,30^{\circ}}$ was not computed. For C3 the "μ-calibration period" was 19 May 2019 00:00 – 24 May 2019 00:00, during the "snow-free" period after snow melt for all $\theta = \{30^{\circ}, \ldots, 60^{\circ}\}$. For C4, it was 11 October 2019 00:00 – 3 November 2019 00:00, during the "snow-free" period before snow onset for all $\theta = \{30^{\circ}, \ldots, 60^{\circ}\}$.

The second step computes the time-series of $T_{\mathrm{R}}^{p}(\theta)$ from $\mu_{\mathrm{R}}^{p,\theta}$ and the measurements $T_{\mathrm{B}}^{p,\phi_{\mathrm{R}}}(\theta)$ and $T_{\mathrm{B}}^{p,\phi_{\mathrm{N}}}(\theta)$ acquired throughout the campaign. Equation (10) is solved for $T_{\mathrm{R}}^{p}(\theta)$ and

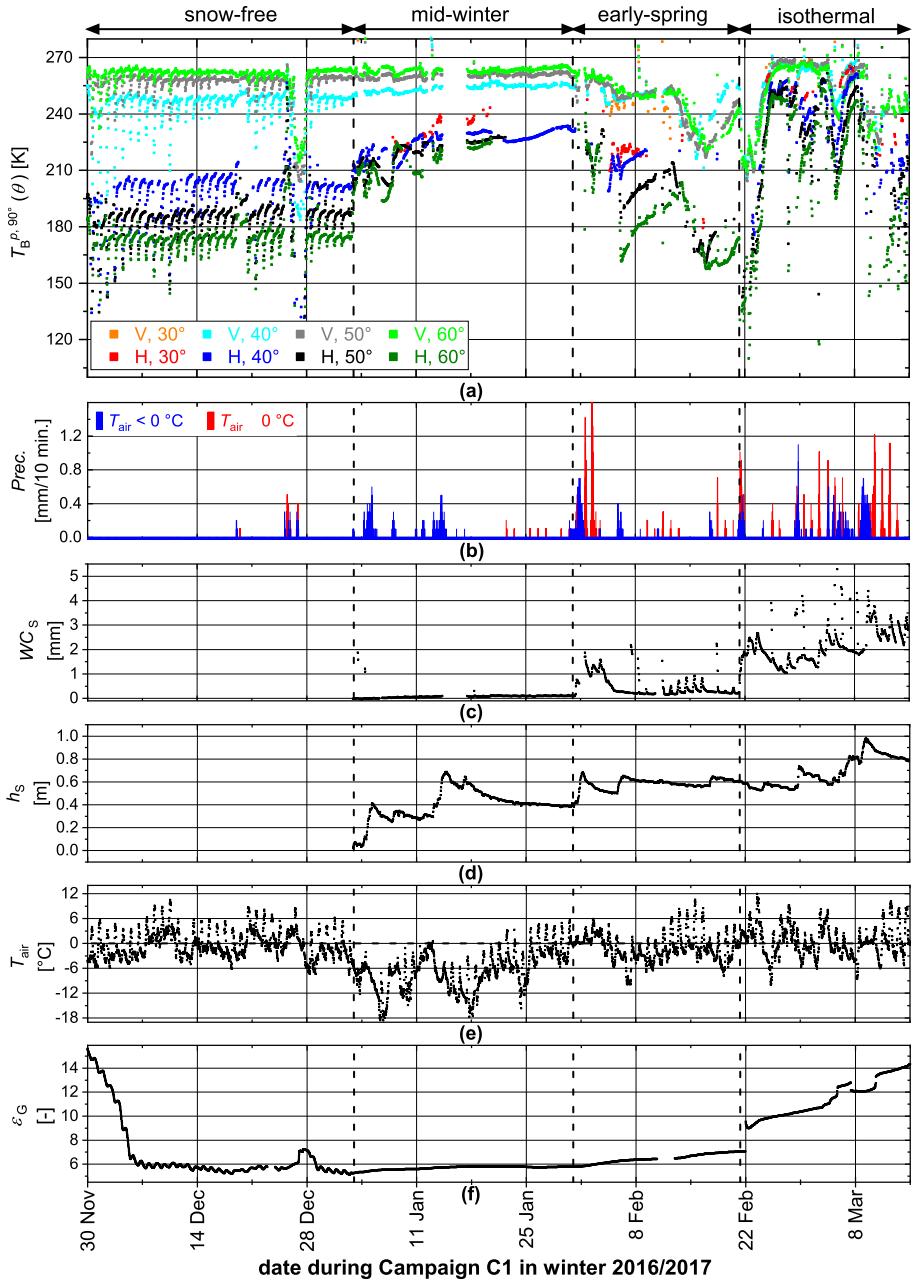

Fig. 3. Measurements conducted during winter Campaign C1 (2016/2017). (a) Brightness temperatures $T_B^{p,90^\circ}(\theta)$ over "natural area" at $\phi = 90^\circ$ (polarization $p = \{\text{H,V}\}$ and nadir observation angles $\theta = \{30^\circ, 40^\circ, 50^\circ, 60^\circ\}$ are indicated in the legend); (b) Precipitation (*Prec.*) differentiated according to $T_{\text{air}} \geq 0$ °C (red) and $T_{\text{air}} < 0$ °C (blue); (c) Snow liquid Water-Column WC_S retrieved from $T_R^p(\theta)$ of the "reflector area"; (d) Snow height h_S; (e) air temperature T_{air}; (f) mean Ground permittivity ϵ_G measured along Transect T1(C1) shown in Fig. 2.

the previously calibrated $\mu_R^{p,\theta}$-values are considered as constants during each campaign.

The third step is the actual retrieval of Snow liquid Water-content W_S from $T_R^p(\theta)$. A W_S-retrieval is achieved by minimizing the sum of squared differences between simulated $T_{R,sim}^p(\theta)$ and measurement-based $T_R^p(\theta)$. Accordingly, the W_S is retrieved by minimizing the following cost function:

$$\text{CF}(W_S) = \Sigma_{p,\theta}\left(T_{R,sim}^p(\theta, W_S) - T_R^p(\theta)\right)^2. \quad (11)$$

The single-layer configuration of the L-band-Specific Microwave Emission Model of Layered Snowpacks "LS-MEMLS" [22] is used to simulate $T_{R,sim}^p(\theta, W_S)$ as a function of the retrieval parameter W_S and the auxiliary model parameters: s_S^p, T_S, ρ_S, h_S, T_{air}, and $s_G^p = 1$ representing the reflectivity of the metal-mesh reflector. The respective modeling equations are provided in [27]. Snow temperature is considered consistently as its maximum possible value $T_S = 0$ °C, because for $T_S < 0$ °C, the snowpack is transparent at L-band, and therefore not emitting. In-situ measured Snow density ρ_S is used for the computation of WC_S. Air temperature T_{air} used to simulate T_{sky} is

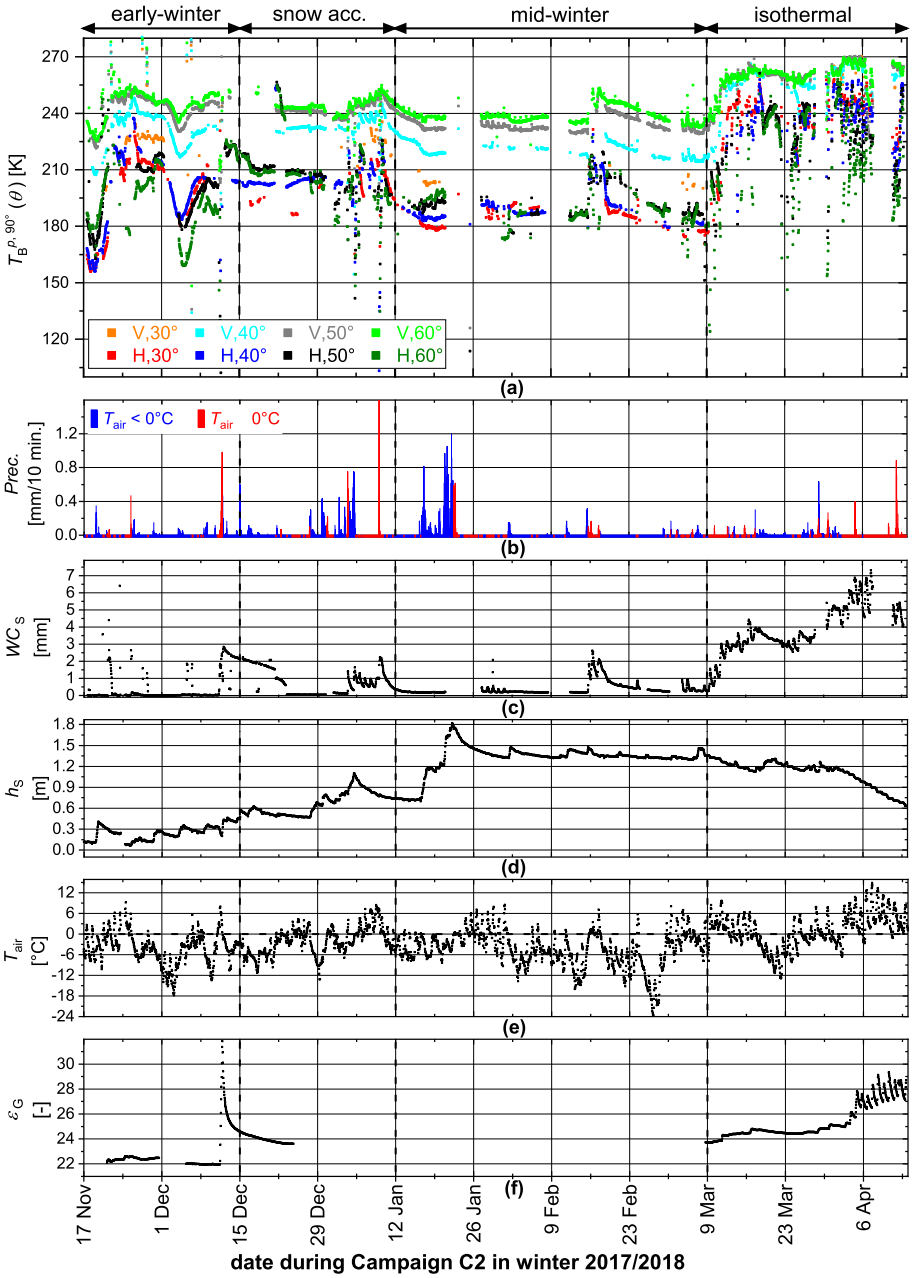

Fig. 4. Measurements conducted during winter Campaign C2 (2017/2018). (a) Brightness temperatures $T_{\mathrm{B}}^{p,90^\circ}(\theta)$ over "natural area" at $\phi = 90^\circ$ (polarization $p = \{\mathrm{H,V}\}$ and nadir observation angles $\theta = \{30^\circ, 40^\circ, 50^\circ, 60^\circ\}$ are indicated in the legend); (b) Precipitation (*Prec.*) differentiated according to $T_{\mathrm{air}} \geq 0$ °C (red) and $T_{\mathrm{air}} < 0$ °C (blue); (c) Snow liquid Water-Column WC_{S} retrieved from $T_{\mathrm{R}}^{p}(\theta)$ of the "Reflector area"; (d) Snow height h_{S}; (e) air temperature T_{air}; (f) mean Ground permittivity ϵ_{G} measured along Transect T1(C1) shown in Fig. 2.

either taken from the PT-100 sensor attached to the ELBARA-II RM (during C1 and C2), or from the AWS (during C3 and C4).

It is noteworthy that W_{S} retrieved with the aforementioned approach is only qualitatively accurate, mostly because of the simplicity of the single-layer microwave emission model used to simulate $T_{\mathrm{R,sim}}^{p}(\theta, W_{\mathrm{S}})$. However, retrieved W_{S} is useful to reliably classify the snowpacks main wetness states, such as dry, moist, and wet. As mentioned earlier, this information is helpful to explore responses of RS signatures to snow melt and wetness variations. The time-series of $T_{\mathrm{R}}^{p}(\theta)$ and weighting-factors $\mu_{\mathrm{R}}^{p,\theta}$ are included in the data package made available.

V. Overview of Measurements

Each of the four conducted winter campaigns lasted several months and covered multiple phases of S-G system states. To simplify the inspection and analysis of L-band Brightness temperatures $T_{\mathrm{B}}^{p,\phi}(\theta)$ response to various SP, we define and consistently use a set of characteristic "phases", which are as follows.

"snow-free": At the beginning or the end of Campaigns, except for C2, measurements were performed in the absence of snow cover. The defining condition for "snow-free" phase is $h_{\mathrm{S}} = 0$ m.

"early-winter": Sometimes the beginning of a stable snow cover period was unclear leading to a period of $h_{\rm S} \leq 0.4$ m where snow height fluctuated between zero and approximately 0.4 m. Air temperature in "early-winter" often rose above 0 °C during the day and precipitation could be both snow and rain. With these varying snow cover conditions and yet nonnegligible effect of thin snow on L-band measurements $T_{\rm B}^{p,\phi}(\theta)$, we define "early-winter" as a separate phase.

"snow accumulation": Also called "acc." in the following graphs, is the period over which Snow height at least doubled from the maximum $h_{\rm S} = 0.4$ m in "early-winter" to >0.8 m. This phase is characterized by gradually decreasing $T_{\rm air}$ and mainly snow precipitation. The duration of the "snow accumulation" phase varies greatly among different winters. During the first Campaigns C1 (winter 2016/2017), it was very short and, therefore, not shown in the corresponding Fig. 3. During winter 2017/2018 (C2), the "snow accumulation" phase lasted for more than a month, as shown in Fig. 4. During the winters 2018/2019 (C3) and 2019/2020 (C4), the respective "snow accumulation" phase lasted around 10 and 14 days as is seen in Figs. 5 and 6, respectively.

"mid-winter": This period is characterized by the stable presence of a generally dry ($W_{\rm S} = 0$ m^{3}m^{-3}) snowpack reaching its maximum seasonal $h_{\rm S}$ with $T_{\rm air} < 0$ °C most of the time.

"early-spring": Increased thermal energy input brought by increasing $T_{\rm air}$ (via convection and conduction) and absorption of sunlight during longer days eventually overcomes ice latent heat and causes partial melt in snow. Accordingly, this phase is characterized by daily fluctuations of $W_{\rm S}$ without rapid decrease in $h_{\rm S}$.

"isothermal": With $T_{\rm air} > 0$ °C during daytime, the snowpack reaches isothermal state at the maximum possible temperature $T_{\rm S} = 0$ °C. The key feature of this phase is that the snowpack does not refreeze overnight, rather due to very high values of $W_{\rm S}$, it becomes opaque at L-band. This phase can take several weeks accompanied by snow and rain precipitations. Liquid water discharge from the snowpack can also influence the underlying Ground permittivity $\epsilon_{\rm G}$.

We acknowledge that the parameter thresholds given in our definitions of different winter "phases" are not strict, rather approximate indicators of the S-G system state. In the following sections, we present $T_{\rm B}^{p,\phi}(\theta)$ at nadir angles $\theta = \{30^\circ, 40^\circ, 50^\circ\}$ such that $T_{\rm B}^{p,\phi}(\theta = 30^\circ)$, $T_{\rm B}^{p,\phi}(\theta = 40^\circ)$, and $T_{\rm B}^{p,\phi}(\theta = 50^\circ)$ are Brightness temperatures averaged over $\theta = \{30^\circ, 35^\circ\}$, $\theta = \{40^\circ, 45^\circ\}$, and $\theta = \{50^\circ, 55^\circ\}$, respectively. The reasons for this averaging are to 1) ensure better statistics when brightness temperatures are partially filtered for RFI, and 2) better readability of data. Furthermore, because of the HPFB of 12° of the used Picket-horn antenna, it is expected that the amount of information contained in these averaged brightness temperatures is nearly the same as the one contained in $T_{\rm B}^{p}(\theta)$ measured at 5° elevation angle intervals.

There exist some gaps in panel (a) of each of the Figs. 3–6 indicating missing $T_{\rm B}^{p,\phi}(\theta)$ for all nadir angles and both polarization. These gaps are almost exclusively due to failed automatic elevation-azimuth positioning of the RM as the result of heavy snowfall and added weight load over the horn antenna.

A. First Campaign (C1, 2016/2017)

Fig. 3 provides an overview of the measurements conducted during C1. $T_{\rm B}^{p,90^\circ}(\theta)$ in Fig. 3(a) is measured over the "natural area" at $\phi = 90^\circ$ as indicated in Fig. 2(a). As shown in Fig. 3(f), average Ground permittivity decreased from $\epsilon_{\rm G} > 14$ at the beginning of C1 to $\epsilon_{\rm G} \approx 6$ by 3 January 2017. This is because a prolonged "snow-free" phase extending to January 2017 accompanied by low $T_{\rm air}$ resulted in frozen ground condition at least to the depth of ∼5 cm of the installed in-situ sensors used to measure $\epsilon_{\rm G}$. In absence of snow cover the ground was exposed to changing air temperature, incoming radiation, and rain. Therefore, $\epsilon_{\rm G}$ fluctuated daily and responded to major changes such as increased soil moisture caused by rain on 26 December 2016 as apparent from Fig. 3(b). Heavy snowfall between 3 and 5 January 2017 introduced a ∼ 0.4-m-thick stable dry snow cover over the site and by 14 January 2017 $h_{\rm S}$ reached ∼ 65% of its maximum seasonal value. This quick accumulation of snow accompanied by consistent $T_{\rm air} < 0$ °C [Fig. 3(e)] and $WC_{\rm S} = 0$ mm [Fig. 3(c)] led to segmenting the beginning of the campaign from the "snow-free" phase straight to the "mid-winter" phase.

Fig. 3(a) shows the clear response of $T_{\rm B}^{p,90^\circ}(\theta)$ to changing emissivity of the observed "natural area" as a result of partial melt/refreeze cycles of the ground. With the appearance of dry snow cover on 3 January 2017, the daily fluctuations in brightness temperature diminish and $T_{\rm B}^{\rm H,90^\circ}(\theta)$ at p=H responds to dry snow with a 14–32 K increase for $\theta = 30^\circ$ to $\theta = 60^\circ$. This effect is also present in $T_{\rm B}^{\rm V,90^\circ}(\theta)$ at p=V but less noticeable. These brightness temperature responses are in line with LS-MEMLS simulations published in [22], and the following theoretical study [23] that laid the ground for snow retrievals based on L-band radiometry. It concluded that: "The fact that dry snow is almost fully transparent at wavelengths around 21 cm does not imply that dry snow can be treated as "invisible" for passive L-band measurements."

From 31 January 2017, the "early-spring" phase starts with $WC_{\rm S}$ first limited to <2 mm and later fluctuating daily between 8 and 20 February 2017. The "isothermal" phase started on 22 February and continued until the end of the campaign with increasing $WC_{\rm S}$ such that the snowpack was consistently wet and mostly opaque at L-band. The liquid water discharge from the snowpack simultaneously increased the moisture of the subnivean Ground and, therefore, increased its permittivity [Fig. 3(f)] from $\epsilon_{\rm G} \approx 6$ to $\epsilon_{\rm G} \approx 14$.

B. Second Campaign (C2, 2017/2018)

Fig. 4 provides an overview of the measurements conducted during C2. This campaign was the only one with no L-band radiometry in "snow-free" phase, as is apparent from $h_{\rm S} > 0$ m shown in Fig. 4(d). Therefore, C2 starts on 17 November 2017 with "early-winter" phase followed by "snow accumulation" phase between 15 December 2017 to 12 January 2018. Due to

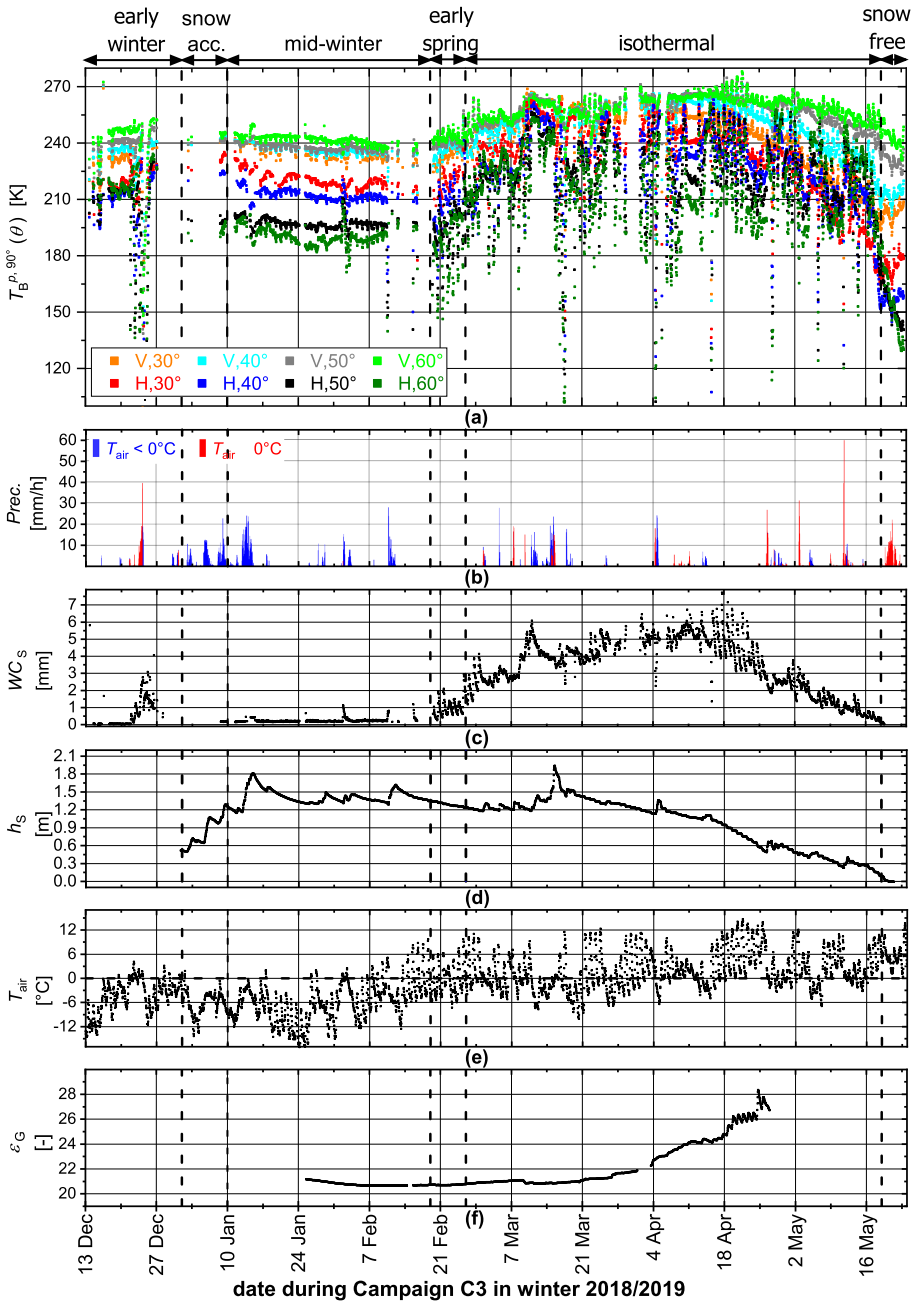

Fig. 5. Measurements conducted during winter Campaign C3 (2018/2019). (a) Brightness temperatures $T_B^{p,90^\circ}(\theta)$ over "natural area" at $\phi = 90^\circ$ (polarization $p = \{H,V\}$ and nadir observation angles $\theta = \{30^\circ, 40^\circ, 50^\circ, 60^\circ\}$ are indicated in the legend); (b) Precipitation (*Prec.*) differentiated according to $T_{air} \geq 0$ °C (red) and $T_{air} < 0$ °C (blue); (c) Snow liquid Water-Column WC_S retrieved from $T_R^p(\theta)$ of the "Reflector area"; (d) Snow height h_S; (e) air temperature T_{air}; (f) mean Ground permittivity ϵ_G measured along Transect T1(C1) shown in Fig. 2.

small Snow height h_S in "early-winter", increased air temperature $T_{air} \gg 0$ °C or precipitation under these conditions (on 25 November 2017, for instance) significantly increased WC_S [Fig. 4(c)]. This situation continued through the "snow accumulation" phase except for 23 December 2017 to 12 January 2018 where the snowpack was temporarily dry. The effect of significant WC_S fluctuations on $T_B^{p,90^\circ}(\theta)$ is easily distinguishable during the "early-winter" phase. Examples include the dip in $T_B^{p,90^\circ}(\theta)$ on 5 December 2017 05:00. At around this time T_{air} was significantly below 0 °C for several days [Fig. 4(e)], and Snow height was just about $h_S \approx 30$ cm [Fig. 4(d)]. Accordingly, Snow liquid Water-Column WC_S has been reduced to an absolute minimum [Fig. 4(c)], implying that the snowpack has become highly transparent. Accordingly, upwelling emission from the unfrozen ground below the snowpack [Fig. 4(f)] dominates measured brightness temperatures. This explains the pronounced dips in $T_B^{V,90^\circ}$ and $T_B^{H,90^\circ}$ by as much as 22 and 50 K to values well comparable to the respective brightness temperatures measured when snow was almost not present ($h_S \leq 10$ cm) over the unfrozen ground at 17 November 2017.

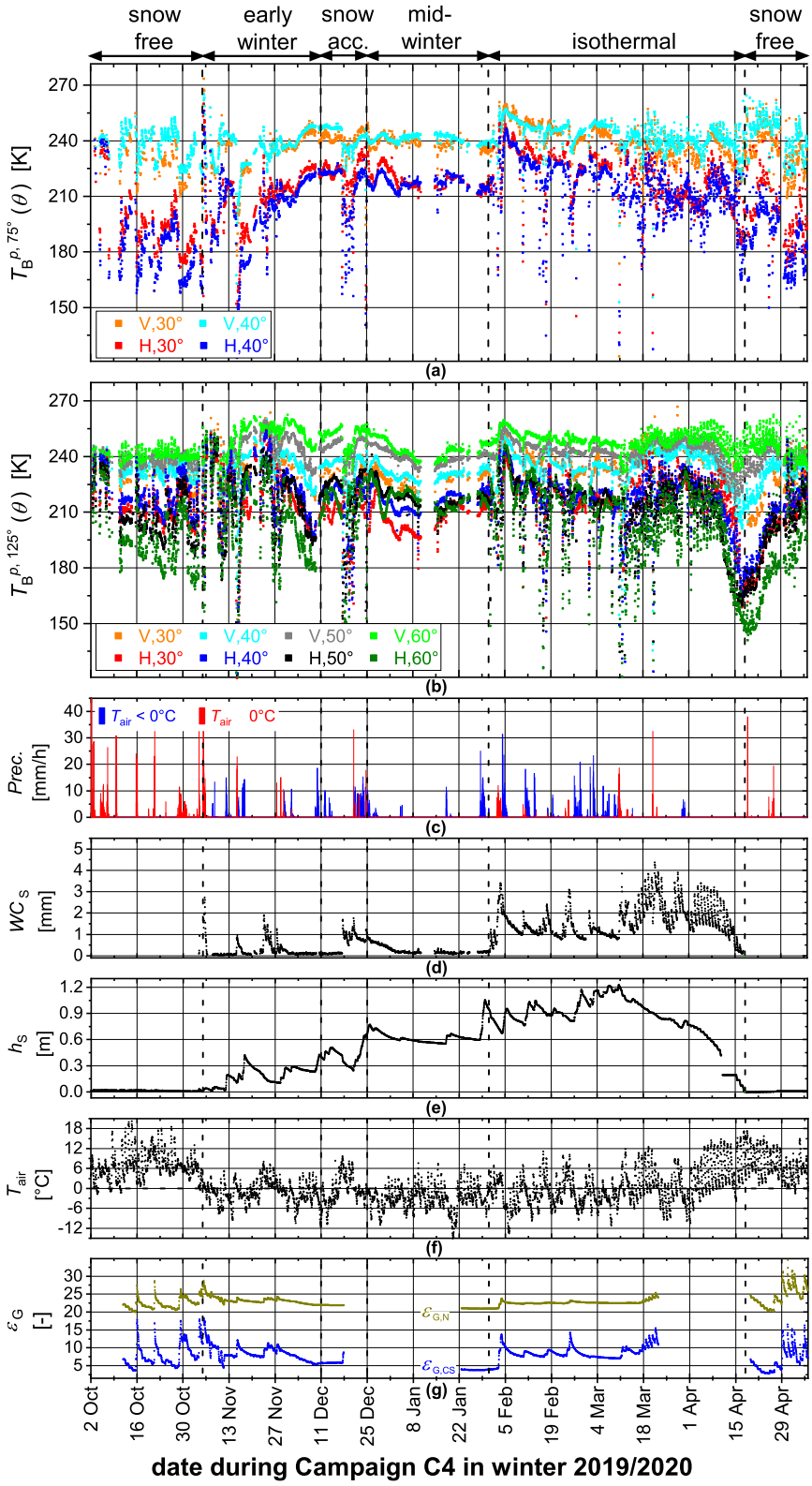

Fig. 6. Measurements conducted during winter Campaign C4 (2019/2020). (a) Brightness temperatures $T_{\mathrm{B}}^{p,75^\circ}(\theta)$ over "charcoal-sand areas" at $\phi = 75°$; (b) Brightness temperatures $T_{\mathrm{B}}^{p,125^\circ}(\theta)$ over "natural areas" at $\phi = 125°$; (c) Precipitation (*Prec.*) differentiated according to $T_{\mathrm{air}} \geq 0°\mathrm{C}$ (red) and $T_{\mathrm{air}} < 0°\mathrm{C}$ (blue); (d) Snow liquid Water-Column WC_{S} retrieved from $T_{\mathrm{R}}^{p}(\theta)$ of the "Reflector area"; (e) Snow height h_{S}; (f) air temperature T_{air}; (g) mean Ground permittivities $\epsilon_{\mathrm{G}} = \epsilon_{\mathrm{G,N}}$ (yellow) and $\epsilon_{\mathrm{G}} = \epsilon_{\mathrm{CS}}$ (blue) measured along Transects T2(C4) and T1(C4), respectively, shown in Fig. 2.

Measured ϵ_{G} in Fig. 4(f) shows 1) the Ground was unfrozen during C2, and 2) even a thin snowpack is sufficient to thermally insulate the subnivean layer.

"Mid-winter" phase stretched from 12 January 2018 to 9 March 2018 where average daily T_{air} was below 0 °C and WC_{S} was mostly 0 mm. The only exception to the latter is 16 and 17 February 2018 where $T_{\mathrm{air}} > 0$ °C accompanied by precipitation [in the form of rain or moist snow marked red in Fig. 4(b)] caused increased Snow liquid Water-content. Careful inspection of WC_{S} [Fig. 4(c)] reveals toothlike fluctuations of Snow liquid Water-Column between 27 and 31 January 2018 in response to daily $T_{\mathrm{air}} > 0$ °C. The L-band brightness temperatures' response to these marginal WC_{S} fluctuations is best visible in $T_{\mathrm{B}}^{\mathrm{V},90^{\circ}}(\theta)$ for $\theta = \{50^{\circ}, 60^{\circ}\}$.

The campaign's last phase was "isothermal" which consisted of positive average daily T_{air} reaching > 12 °C, increasingly higher WC_{S}, and decaying Snow height h_{S}. We have not identified an "early-spring" phase in C2 simply because virtually immediately after the "mid-winter" phase the snowpack became consistently wet and, therefore, isothermal at 0 °C. From 3 April 2018, despite the presence of snow cover, ϵ_{G} in Fig. 4(f) seems highly correlated primarily with daily T_{air} fluctuations such that the peak of ϵ_{G} takes place between three to five hours after maximum T_{air} in the afternoon. This is due to extra liquid water discharged from the snowpack during the accelerated melt in the afternoon.

C. Third Campaign (C3, 2018/2019)

Fig. 5 provides an overview of the measurements conducted during C3. As shown in Table II and in Fig. 5, C3 started on 13 December 2018 with an already existing snow cover of $h_{\mathrm{S}} \approx 0.4$ m. During the "snow accumulation" and "mid-winter" phases, the snowpack grew thicker while average T_{air} dropped below 0 °C. As shown in Fig. 5(c), the snowpack was nearly consistently dry during "mid-winter" phase. In response to consistently dry snow condition, $T_{\mathrm{B}}^{p,90^{\circ}}(\theta)$ became stable and free of strong fluctuations. The "early-spring" phase started on 19 February 2019 with daily snowpack melt/refreeze cycles. The "isothermal" phase was exceptionally long in that it lasted almost three months from 26 February 2019 to 19 May 2019. According to Fig. 5(c), during this phase increased WC_{S} implies opaqueness of the snowpack at L-band. However, constant snow melt was partially compensated for by snow falls [Fig. 5(b)], during the "isothermal" phase whose signatures are best visible in local peaks of h_{S} in Fig. 5(d), for example, on 15 March 2019 and 5 April 2019.

Snow melt was not perfectly homogeneous over the site; nevertheless, AWS measurements and photographic documentation indicate 19 May 2019 as the complete snow melt date. In response to complete snow melt, $T_{\mathrm{B}}^{p,90^{\circ}}(\theta)$ at both polarization falls to significantly lower values with p=H expressing a stronger effect for example with $T_{\mathrm{B}}^{\mathrm{H},90^{\circ}}(\theta = 60^{\circ})$ dropping by 50 K from 16 to 21 May 2019.

Despite the data gaps in ϵ_{G} due to technical malfunctioning of the DT80 data logger, Fig. 5(f) shows that the subnivean ground was unfrozen during the entire campaign with an average $\epsilon_{\mathrm{G}} \approx 21$ until the end of March 2019. With the melt water from the snowpack percolating down to the ground, Ground permittivity increased to $\epsilon_{\mathrm{G}} > 26$. Between 18 and 26 April 2019, ϵ_{G} fluctuated daily, which was the result of accelerated snow melt during the peak air temperatures.

It is noteworthy that in response to the varying WC_{S}, Brightness temperatures $T_{\mathrm{B}}^{p,90^{\circ}}(\theta)$ fluctuate. However, in "isothermal" phase with consistent $WC_{\mathrm{S}} > 0$ mm such a one-to-one traceability is missing. The interpretation of $T_{\mathrm{B}}^{p,90^{\circ}}(\theta)$ time-series during the "isothermal" phase is complicated because the permanent presence of increasing snow liquid-water and its changing distribution across the snow profile causes partial or complete opaqueness at L-band. Nevertheless, the response of $T_{\mathrm{B}}^{p,90^{\circ}}(\theta)$ to some major changes in the S-G system can be identified.

D. Fourth Campaign (C4, 2019/2020)

Fig. 6 provides an overview of the measurements conducted during C4. This last Campaigns was the most comprehensive of all in that it was both the longest and encompassed most of the winter phases defined. Fig. 6(a) and (b) shows the time-series of $T_{\mathrm{B}}^{p,\phi}(\theta)$ measured over "charcoal-sand area" at $\phi = 75^{\circ}$ and over the "natural area" at $\phi = 125^{\circ}$, respectively. In Fig. 6(a), only $T_{\mathrm{B}}^{p,75^{\circ}}(\theta)$ at $\theta = 30^{\circ}$ and $\theta = 40^{\circ}$ are shown because as illustrated in Fig. 2(b), the "charcoal-sand area" was designed to fully cover L-band RMs -9 dB FPs associated with $30^{\circ} \lesssim \theta \leq 45^{\circ}$. It is evident from Fig. 6, especially during "snow-free" and "mid-winter" phases, polarization differences in brightness temperatures are more pronounced for $T_{\mathrm{B}}^{p,75^{\circ}}(\theta)$ over the "charcoal-sand area" than for $T_{\mathrm{B}}^{p,125^{\circ}}(\theta)$ measured over the "natural area." This is best visible during the "snow-free" phase at the beginning of the campaign where for a given nadir angle θ differences $T_{\mathrm{B}}^{\mathrm{V},75^{\circ}}(\theta) - T_{\mathrm{B}}^{\mathrm{H},75^{\circ}}(\theta)$ over the "charcoal-sand area" is ~ 40 K [Fig. 6(a)] while corresponding differences $T_{\mathrm{B}}^{\mathrm{V},125^{\circ}}(\theta) - T_{\mathrm{B}}^{\mathrm{H},125^{\circ}}(\theta)$ over the "natural area" is ~ 30 K [Fig. 6(b)]. This is a direct effect of impedance matching and lower surface roughness provided by the "charcoal-sand area" compared to the "natural area."

C1 and C4 are similar in that they both start with the "snow-free" phase. However, as seen in Fig. 6(f), air temperature was virtually constantly above $T_{\mathrm{air}} = 0$ °C, which prevented the ground from freezing. Correspondingly, mean Ground permittivities of "Natural area" (N) [measured with sensors along T2(C4) and T3(C4) in Fig. 2] are $\epsilon_{\mathrm{G,N}} > 20$ [Fig. 6(g)] and, therefore, prove the unfrozen state of ground. In contrast, mean permittivities $\epsilon_{\mathrm{G,CS}}$ within the "Charcoal-Sand area" (CS) are considerably lower, sometimes $\epsilon_{\mathrm{G,CS}} < 5$. However, this does not mean that the "charcoal-sand area" froze at any time; instead, the generally low $\epsilon_{\mathrm{G,CS}}$ are due to the low water-holding capacity of the surface layer of this area.

Both permittivity records, $\epsilon_{\mathrm{G,N}}$ and $\epsilon_{\mathrm{G,CS}}$, fluctuate in response to precipitations such as on 16, 21, and 29 October 2019 during the "snow-free" period before snow onset. During the "early winter" phase, in-situ $\epsilon_{\mathrm{G,N}}$ and $\epsilon_{\mathrm{G,CS}}$ respond to liquid water brought by major precipitations at $T_{\mathrm{air}} > 0$ °C (for example, on 15 November 2019) and increased WC_{S} (for example, on 23–25 November 2019). Fig. 6(g) shows that

Fig. 7. Pictures from the instrument surveillance camera on (a) 19 April 2020 10:38 CET after the snow melt, and (b) 7 May 2020 10:38 CET near the end of the Campaign C4. The vegetation growth is evident in panel (b).

from approximately 30 November 2019 ground permittivities of the "natural area" and the "charcoal-sand area" ceased their fluctuations and by the middle of the "snow accumulation" phase they had settled to $\epsilon_{\mathrm{G,N}} \approx 21.8$ and $\epsilon_{\mathrm{G,CS}} \approx 5.8$, respectively. Despite the gap in the ground permittivities, the next available records on 23 January 2020 in "mid-winter" phase confirm that in presence of thermally insulating snow, subnivean permittivity was stable. The time-series of WC_{S} in Fig. 6(d) shows that the "mid-winter" phase is immediately followed by "isothermal" phase with WC_{S} rapidly increasing to high values making the snowpack opaque even for L-band observations.

According to Fig. 6(e), the "isothermal" phase ended with a quick melt enforced with consistent $T_{\mathrm{air}} > 0$ °C such that between 10 and 18 April 2020, h_{S} dropped from ∼0.45 m to zero. The signature of this quickly disappearing snow cover is visible in $T_{\mathrm{B}}^{p,75^\circ}(\theta)$ over the "charcoal-sand area" [Fig. 6(a)] and in $T_{\mathrm{B}}^{p,125^\circ}(\theta)$ over "natural area" [Fig. 6(b)]. For example, $T_{\mathrm{B}}^{\mathrm{H},75^\circ}(40^\circ)$ and $T_{\mathrm{B}}^{\mathrm{H},125^\circ}(60^\circ)$ drop by ~ 50 K and ~ 64 K, respectively, in the aforementioned period. It is noteworthy that after complete snow melt, $T_{\mathrm{B}}^{p,125^\circ}(\theta)$ [Fig. 6(b)] especially at p=H, starts increasing. Given the increased $T_{\mathrm{air}} \gg 0$ °C and snow-free conditions, the vegetation started growing on natural soil. Photographic proof of this vegetation growth is provided in Fig. 7. Both photos were automatically taken at 10:38 CET after the end of the "isothermal" phase (19 April 2020) and at the end of campaign (7 May 2020). Since the "snow-free" phase after snow clearance lasted for ∼20 days, the effect of growing vegetation on $T_{\mathrm{B}}^{p,125^\circ}(\theta)$ is noticeable. Fig. 7(b) shows that by the end of the campaign even the "reflector area" at $\phi = 180^\circ$ [Fig. 2(b)] is covered with green grass, which grew through the metal-mesh grid. Vegetation did not grow over the artificially created "charcoal-sand area"; therefore, $T_{\mathrm{B}}^{p,75^\circ}(\theta)$ does not exhibit an increasing trend toward the end of C4.

VI. Multiyear Overview of Angular Dependence of $T_{\mathrm{B}}^{p,\phi}(\theta)$

The time-series of measured L-band brightness temperatures for each campaign was presented and discussed in Section V. Alternatively, Fig. 8 provides a summary overview of $T_{\mathrm{B}}^{p,\phi}(\theta)$ for all four campaigns as a function of nadir angle θ. The graphs in Fig. 8 are based on $T_{\mathrm{B}}^{p,\phi}(\theta)$ measured for azimuth angles $\phi = \{90^\circ, 90^\circ, 90^\circ, 125^\circ\}$ along "natural areas" in Campaigns {C1,C2,C3,C4} (Fig. 2). Each column in Fig. 8 refers to one Campaign (C) and the title above the top graph in each column indicates the Campaign number C#, ground freeze/thaw condition (frozen or unfrozen), and the azimuth angles ϕ of FPs over "natural area" where radiometry was conducted. The first, second, and third rows in Fig. 8 refer to "snow-free" ($h_{\mathrm{S}} \approx 0$ m), "dry-snow" ($h_{\mathrm{S}} > 0.05$ m and $0\ \mathrm{mm} < WC_{\mathrm{S}} < 0.2$ mm), and "wet-snow" ($h_{\mathrm{S}} > 0.05$ m and $WC_{\mathrm{S}} > 0.5$ mm) conditions, respectively. Accordingly, for each nadir angle θ in each panel, the average $\langle T_{\mathrm{B}}^{p,\phi}(\theta) \rangle$ for p={H,V} is computed and plotted. The vertical bars at each data point indicate the standard deviation of $T_{\mathrm{B}}^{p,\phi}(\theta)$ and are indicative of the variability of brightness temperatures for a given scenario. For example, since the only condition for "snow-free" graphs is the absence of snow cover ($h_{\mathrm{S}} \approx 0$ m), $\langle T_{\mathrm{B}}^{p,\phi}(\theta) \rangle$ can still refer to nighttime and daytime conditions as well as different meteorological conditions such as precipitation which may change FP emissivity as discussed in Section VII. In the following, we highlight a few key observations based on the angular behavior of $\langle T_{\mathrm{B}}^{p,\phi}(\theta) \rangle$ shown in Fig. 8.

The "snow-free" graphs in Fig. 8 show that when the ground is frozen [C1 in Fig. 8(a)] $T_{\mathrm{B}}^{p,\phi}(\theta)$ is larger than what is measured for unfrozen ground conditions [C3 and C4 in Fig. 8(g) and (j)]. Due to smaller permittivities ϵ_{G} of frozen Ground compared to ϵ_{G} of moist, unfrozen ground this was expected and confirmed by LS-MEMLS simulations [23]. In Campaigns C1, C3, and C4 where "snow-free" conditions were available, the comparison between "snow-free" and "dry-snow" graphs [Fig. 8(a) and (b) for C1, Fig. 8(g) and (h) for C3, and Fig. 8(j) and (k) for C4] show that dry snow cover increases $T_{\mathrm{B}}^{p,\phi}(\theta)$. Impedance matching caused by the dry snowpack is the reason for higher brightness temperatures during "dry snow" periods than during "snow-free" periods. As anticipated by LS-MEMLS simulations, this increasing effect is stronger at p=H than at p=V.

Comparison between the "dry-snow" and "wet-snow" graphs in each campaign indicates increased brightness temperature

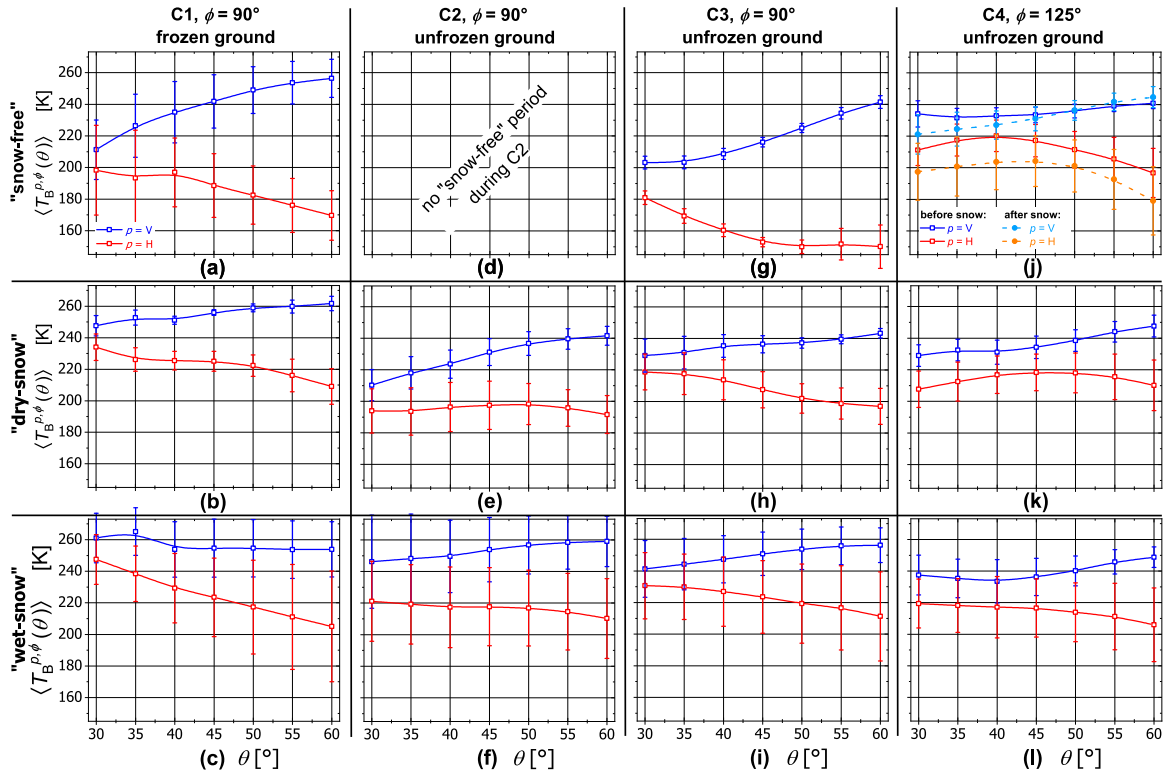

Fig. 8. Summary overview of measured dependence of $\left\langle T_{\mathrm{B}}^{p,\phi}(\theta)\right\rangle$ over "natural areas" averaged over the time-periods identified as "snow-free", "dry-snow", "wet-snow" (rows labeled at the left) during the winter Campaigns C1 (2016/2017), C2 (2017/2018), C3 (2018/2019), and C4 (2019/2020) (columns labeled at the top). Bars at each data point indicate the standard deviation during the indicated winter periods and campaigns.

variability for wet snow conditions evidenced by larger error bars at each nadir angle θ and for both polarization p={H,V}. To understand this observation, we first reiterate that dry snow does not have noticeable self-emission at L-band; therefore, dry snow cover influences the observed brightness temperatures via impedance matching and refraction effects tuned with snow density. However, in presence of liquid water, snowpack starts to emit at L-band and even small variations of Snow liquid Water-content (for instance $W_{\mathrm{S}} < 1\%$) can significantly change the snow cover emissivity. As shown in [27], even the W_{S} distribution pattern across a snow profile can influence the observed $T_{\mathrm{B}}^{p}(\theta)$. Averaged $\langle T_{\mathrm{B}}^{p,\phi}(\theta)\rangle$ reported in Fig. 8(c), (f), (i), and (l) includes measurements in various times and thus a wide range of snow cover properties. As a result, the variability of $T_{\mathrm{B}}^{p,\phi}(\theta)$ is larger for wet snow cover conditions.

Fig. 8 and its brief analysis in this section offer an example of how the measurements from C1-C4 in Davos-Laret site can be examined from multiple points of view. The inspection of data in the time domain (Section V) and the angular domain (Section VI) presents different observations which are possible only by changing the analysis domain.

VII. Effect of Precipitation on Brightness Temperature

A. Modeled Case

Precipitation can generally alter the existing snow cover properties in two main forms: First, dry snow precipitation at $T_{\mathrm{air}} < 0\ ^{\circ}\mathrm{C}$ increases snow height h_{S} and creates a layer of fresh snow atop the snowpack with noticeably lower density ρ_{S} than the rest of the snow profile. Since dry snow is virtually lossless at L-band (penetration depth is > 100 m [5], [21]), the comparably small change in h_{S} does not affect Brightness temperatures $T_{\mathrm{B}}^{p}(\theta)$ of a ground covered with dry snow. However, as shown in [22], dry snow influences $T_{\mathrm{B}}^{p}(\theta)$ via refraction and impedance matching, which is most important at the lower and the upper bound of the snowpack. The second form of snowpack alteration due to precipitation is caused by rain or wet snow precipitation when $T_{\mathrm{air}} \geq 0\ ^{\circ}\mathrm{C}$. Rain or wet snowfall introduces increased Snow liquid Water-content W_{S} on the surface of the snowpack. Light rain may initially increase W_{S} in the snowpack surface-layer while stronger or long-lasting rain may infiltrate the snowpack. However, it is obvious that precipitation in any form (dry- or wet snow, or rain) changes the microwave emissivity of the snow-covered ground. Effects of W_{S} on $T_{\mathrm{B}}^{p}(\theta)$ were investigated for multiple scenarios of wetness distribution across the snow profile [27]. In a wet precipitation scenario, if it happens to be wet snow, we neglect the increased h_{S} and possibly lower ρ_{S} atop the snowpack because the major influential parameter is propagation losses introduced by $W_{\mathrm{S}} > 0\ \mathrm{m^3 m^{-3}}$.

First, we present the comparative response of $T_{\mathrm{B,sim}}^{p}(\theta)$ to dry and wet snow precipitation simulated (sim) with LS-MEMLS and shown in Fig. 9. The bold gray lines in Fig. 9 consistently refer to the situation before precipitation (dry uniform snowpack). The red and green dotted lines, in panel (a) and (b), respectively, refer to simulations of brightness temperature for a snowpack

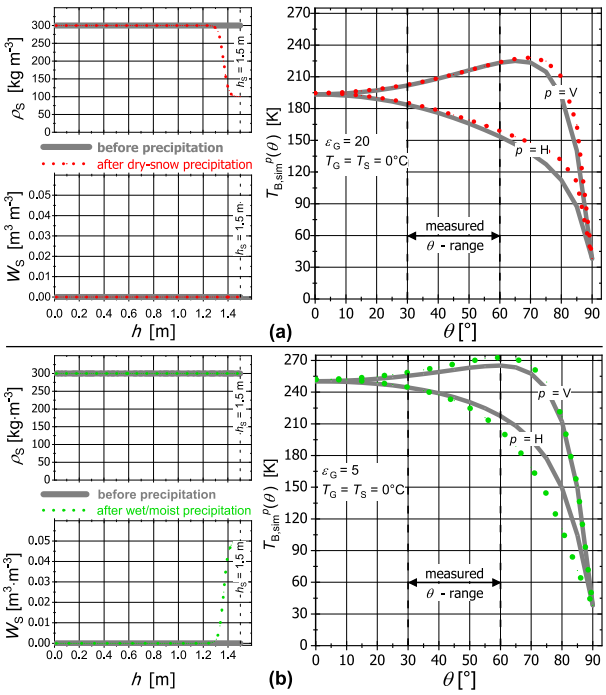

Fig. 9. Simulated responses of Brightness temperatures $T^{p}_{\mathrm{B,sim}}(\theta)$ to (a) dry snow precipitation, and (b) to rain or wet/moist snow precipitation. Respective profiles $\rho_{\mathrm{S}}(h)$ and $W_{\mathrm{S}}(h)$ of Snow density and Snow liquid Water-content are shown in the left parts of panels (a) and (b). The bold gray lines consistently refer to the situation before precipitation (dry uniform snowpack). Red and green dotted lines in (a) and (b) refer to $T^{p}_{\mathrm{B,sim}}(\theta)$ for a snowpack modified by dry and wet/moist precipitation, respectively.

modified with precipitation (light dry snow ($\rho_{\mathrm{S}} = 100\ \mathrm{kg\,m^{-3}}$, $W_{\mathrm{S}} = 0.00\ \mathrm{m^3 m^{-3}}$), or wet snow ($W_{\mathrm{S}} = 0.05\ \mathrm{m^3 m^{-3}}$) in its upper part [profiles $\rho_{\mathrm{S}}(h)$ and $W_{\mathrm{S}}(h)$ shown in the left parts of Fig. 9]. The nadir angle range $30^\circ \leq \theta \leq 60^\circ$ of L-band brightness temperatures measured at the Davos-Laret site is indicated in the right parts of Fig. 9(a) and (b).

To simulate the impact of dry snow precipitation on $T^{p}_{\mathrm{B,sim}}(\theta)$, we use Fermi-Dirac function (Section 5.2 in [55]) to create a Snow density profile $\rho_{\mathrm{S}}(h)$ with decreasing density in the upper part of the snowpack [Fig. 9(a)]. Concretely, we have chosen a snowpack of total height $h_{\mathrm{S}} = 1.5$ m with densities $\rho_{\mathrm{S}}(0) = 300\ \mathrm{kg\,m^{-3}}$ and $\rho_{\mathrm{S}}(h_{\mathrm{S}}) = 100\ \mathrm{kg\,m^{-3}}$ at the bottom and at the top, respectively. Transition height h^* defined by $\rho_{\mathrm{S}}(h^*) = (\rho_{\mathrm{S}}(0) + \rho_{\mathrm{S}}(h_{\mathrm{S}}))/2 = 200\ \mathrm{kg\,m^{-3}}$ is assumed at height $h^* = 0.9 \cdot h_{\mathrm{S}} = 1.35$ m. The profile $W_{\mathrm{S}}(h)$ of Snow liquid Water-content [Fig. 9(a)] is considered as $W_{\mathrm{S}}(h) = 0\ \mathrm{m^3 m^{-3}}$ to represent dry snow precipitation. Furthermore, ground is assumed to be unfrozen ($\epsilon_{\mathrm{G}} = 20$). Simulated $T^{p}_{\mathrm{B,sim}}(\theta)$ shown in the right panel of Fig. 9(a) demonstrate that the light snow atop the snowpack causes an observation angle-dependent increase in $T^{p}_{\mathrm{B,sim}}(\theta)$ (red) compared to $T^{p}_{\mathrm{B,sim}}(\theta)$ (bold gray) simulated for the situation before dry snow precipitation. At horizontal polarization p=H, this increase is stronger at larger nadir angles in the range of $20^\circ \leq \theta \leq 85^\circ$ where $T^{\mathrm{H}}_{\mathrm{B,sim}}(\theta)$ (red) is increased by ~ 2 K and ~ 24 K, respectively. At p=V, this increase is only distinguishable at $60^\circ \leq \theta \leq 85^\circ$. The reason why light dry snow atop the snowpack increases brightness temperature is the decreased reflectivity at the snowpack surface, which corresponds to increased emissivity and, therefore, higher $T^{p}_{\mathrm{B,sim}}(\theta)$.

The simulated impact on $T^{p}_{\mathrm{B,sim}}(\theta)$ induced by rain or wet/moist snow precipitation is demonstrated with Fig. 9(b). To mimic this situation, the uniform Snow density profile $\rho_{\mathrm{S}}(h) = 300\ \mathrm{kg\,m^{-3}}$ is considered. The profile $W_{\mathrm{S}}(h)$ of Snow liquid Water-content representing dry snow at the snowpack bottom ($W_{\mathrm{S}}(0) = 0\ \mathrm{m^3 m^{-3}}$) and wet snow at the top of the snowpack ($W_{\mathrm{S}}(h_{\mathrm{S}}) = 0.05\ \mathrm{m^3 m^{-3}}$) is again represented by a Fermi-Dirac function. It takes the value $W_{\mathrm{S}}(h^*) = (W_{\mathrm{S}}(0) + W_{\mathrm{S}}(h_{\mathrm{S}}))/2 = 0.025\ \mathrm{m^3 m^{-3}}$ at the transition height $h^* = 0.9{\cdot}h_{\mathrm{S}} = 1.35$ m, meaning that the wet snow layer extends over the top $h_{\mathrm{S}} - h^* = 0.15$ m of the snowpack of height $h_{\mathrm{S}} = 1.5$ m. The right panel in Fig. 9(b) shows that moist snow atop the snowpack increases $T^{p}_{\mathrm{B,sim}}(\theta)$ (green) at vertical polarization consistently by ≥ 8 K for $30^\circ \leq \theta \leq 60^\circ$. However, at horizontal polarization, the corresponding response is the opposite, meaning $T^{\mathrm{H}}_{\mathrm{B,sim}}(\theta)$ (green) tends to decrease as a result of the presence of moist snow in the uppermost part of the snowpack. For $\theta \lesssim 40^\circ$, the moist top layer causes a marginal increase (~ 1.5 K) while for $40^\circ \lesssim \theta \leq 60^\circ$, the response in $T^{\mathrm{H}}_{\mathrm{B,sim}}(\theta)$ (green) is decreasing and significantly stronger (up to ~ 20 K).

Measurement-based examples confirming the above presented model-based sensitivities of brightness temperatures to dry and wet snow precipitation and rain are provided in the subsequent section.

B. Experimental Investigation

An example experimental observation of the effect of dry snow precipitation on L-band brightness temperatures is shown in Fig. 10 specifically with gray shadings. This observation was made between 26 January 2019 and 28 January 2019 12:00 in Campaign C3.

Snow liquid Water-Column WC_{S} shown in Fig. 10(c) demonstrates that the snowpack was dry ($WC_{\mathrm{S}} = 0$ mm) while air temperature [Fig. 10(d)] was $T_{\mathrm{air}} < -4\ ^\circ$C at the time of precipitation [Fig. 10(b)] indicating dry snowfall. The latter started around 27 January 2019 21:00, reached its maximum intensity at midnight, and was over by 28 January 2019 02:00. The Brightness temperatures $T^{p,\phi}_{\mathrm{B}}(\theta)$ at p={H,V} shown in Fig. 10(a) are measured for "natural area" FPs at the azimuth angle $\phi = 90^\circ$ in C3 [Fig. 2(a)] and elevation angles $\theta = \{30^\circ, 40^\circ, 50^\circ, 60^\circ\}$.

Fig. 10(a) shows that $T^{\mathrm{H},90^\circ}_{\mathrm{B}}(60^\circ)$ increases by ~ 5.4 K from the start of precipitation until its peak intensity. This effect is increasingly limited for lower θ relative to nadir (steeper observation directions). However, as predicted by the LS-MEMLS simulations in Section VII-A for $30^\circ \leq \theta \leq 60^\circ$, the dry snow precipitation effect is negligible for p=V.

It is noteworthy that dry snow precipitation effect is most notable when there is a heavy snowfall, which quickly forms a distinct lower density layer on top. When the precipitation is prolonged, such as on 26 January 2019 in Fig. 10(b), the effect on $T^{p,\phi}_{\mathrm{B}}(\theta)$, while present, is hardly noticeable. One reason is the gravimetric snowpack compression, which at slow precipitation rates avoids the formation of a top low-density layer.

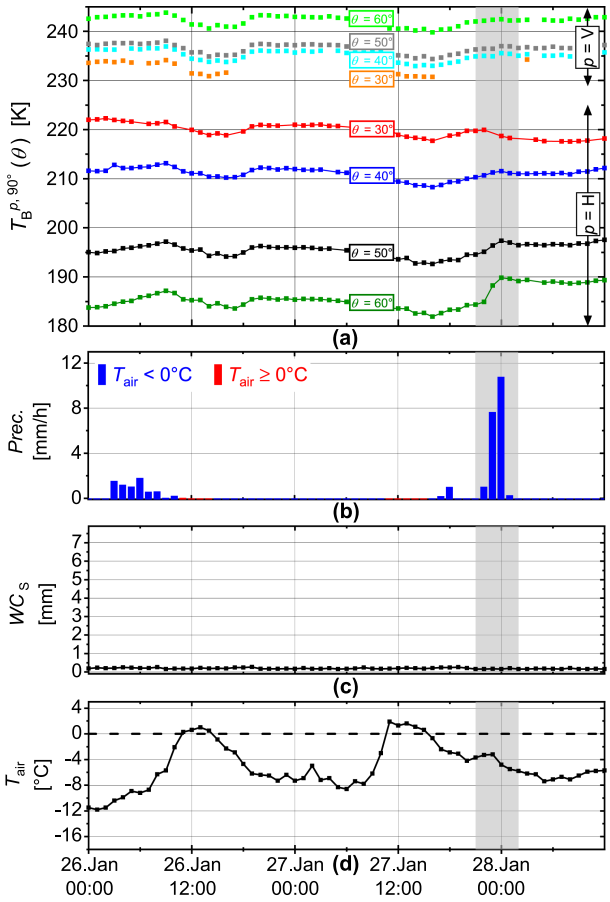

Fig. 10. The 2.5 days of measurements during Campaign C3 including dry snowfall on dry snowpack. (a) Brightness temperatures $T_{\mathrm{B}}^{p,90^\circ}(\theta)$ measured for "natural area" FPs at the azimuth angle $\phi = 90^\circ$ and nadir angles $\theta = \{30^\circ, 40^\circ, 50^\circ, 60^\circ\}$; (b) Precipitation (*Prec.*); (c) Snow liquid Water-Column WC_{S}, and (d) air temperature T_{air}.

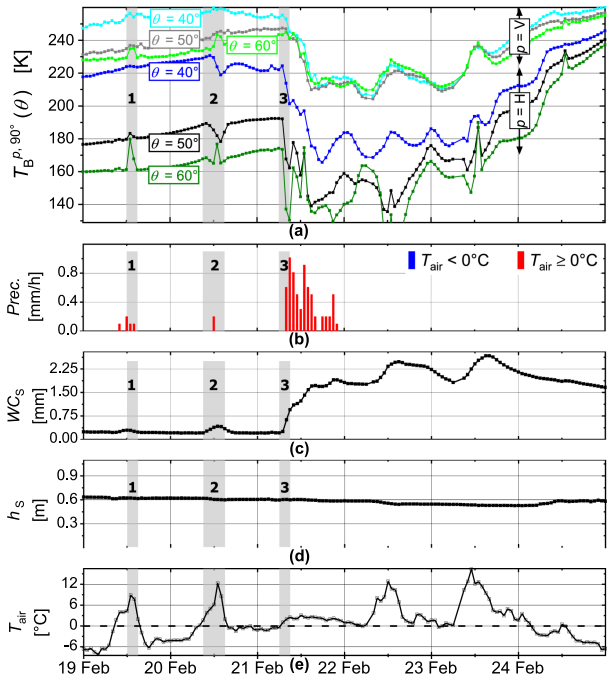

Fig. 11. 5 days of measurements during C1 including wet/moist snowfall on dry snowpack. (a) Brightness temperatures $T_{\mathrm{B}}^{p,90^\circ}(\theta)$ measured for "natural area" FPs at the azimuth angle $\phi = 90^\circ$ and nadir angles $\theta = \{30^\circ, 40^\circ, 50^\circ, 60^\circ\}$; (b) Precipitation (*Prec.*); (c) Snow liquid Water-Column WC_{S}, and (d) air temperature T_{air}.

Fig. 11 provides three consecutive examples of the effect of wet precipitation on L-band Brightness temperatures $T_{\mathrm{B}}^{p,90^\circ}(\theta)$ (p={H,V}, and $\theta = \{30^\circ, 40^\circ, 50^\circ, 60^\circ\}$) measured between 19 and 25 February 2017 in Campaign C1. These examples are highlighted with gray shading across all figure panels and numbered for reference. First, Fig. 11(d) shows that none of the presented precipitations resulted in noticeable change in h_{S} implying that they were either rain on snow or wet snow with no tangible effect on snow height. Fig. 11(b) and (c) show that wet precipitation in case 1 causes a short-term detectable increase in Snow liquid-Water Column WC_{S} [Fig. 11(c)], which falls back to $WC_{\mathrm{S}} = 0$ mm indicating snowpack refreezing. Fig. 11(a) shows that in response to this short-term increased $0\ \mathrm{mm} < WC_{\mathrm{S}} \leq 0.3\ \mathrm{mm}$, $T_{\mathrm{B}}^{p,90^\circ}(\theta)$ at both polarization increases and then returns to preprecipitation level. This effect is distinctly visible in Fig. 11(a) for $T_{\mathrm{B}}^{\mathrm{H},90^\circ}(60^\circ)$ with ~ 20 K. This experimental observation is in line with simulations presented in [27, Fig. 10], which shows an initial increase in brightness temperature for small values of WC_{S} followed by dropping brightness temperature for larger snow liquid water-column.

In case 2, the snow wetness introduced via precipitation reaches $WC_{\mathrm{S}} = 0.4$ mm. Inspection of the grey shaded part of Fig. 11(a) related to case 2 reveals an initial increase for $T_{\mathrm{B}}^{\mathrm{H},90^\circ}(\theta = \{40^\circ, 50^\circ\})$ followed by a drop in brightness temperatures and finally the gradual recovery. This feature is not seen in $T_{\mathrm{B}}^{p,90^\circ}(60^\circ)$ for which the response to increased WC_{S} is solely an increase in brightness temperature. This is thought to be due to the spatial heterogeneities in the largest RM FP area associated with $\theta = 60^\circ$. Case 3 involves a strong prolonged wet precipitation accompanied by about 2.5 days of $T_{\mathrm{air}} > 0$ °C. Accordingly, only the first two hours are considered here starting from 21 February 2017 08:00 where precipitation introduces $WC_{\mathrm{S}} = 0.8$ mm. This quick wetting of the snowpack's surface and the measurement limited temporal resolution of one hour explains the immediately decreasing response of $T_{\mathrm{B}}^{p,90^\circ}(\theta)$ without the initial marginal increase, as predicted by simulations in [27].

This strong precipitation and positive air temperature transfer the snowpack from "early-spring" phase with fluctuating snow melt/refreeze cycles to "snow-melt" phase with consistent $WC_{\mathrm{S}} > 0$ mm. One must note that for such high snow liquid water-columns the analysis of $T_{\mathrm{B}}^{p,90^\circ}(\theta)$ with respect to S-G SPs becomes exceedingly difficult. Nevertheless, the clear post-case 3 trend in Fig. 11 is gradually increasing $T_{\mathrm{B}}^{p,90^\circ}(\theta)$ after 23 February 2017 12:00 in response to partial refreezing of the snowpack (decreasing WC_{S}).

Simulations presented in Section VII-A and in [27] as well as experimental examples, such as in Fig. 11, indicate the complexity of the L-band brightness temperatures' response to snow wetness and melt. Therefore, the accuracy of snow melt detection methods, which are solely based on brightness temperature thresholds and/or air temperature measurements,

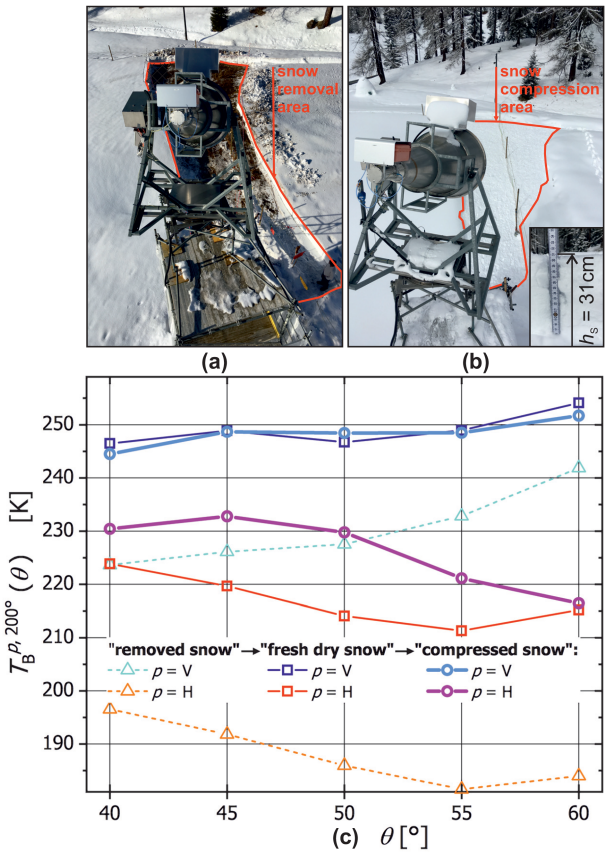

Fig. 12. Results of the snow removal and compression experiment performed during campaign C1. (a) Removal of dry snow cover over ELBARA-IIs −9 dB FPs at $\phi = 200^\circ$ and $35^\circ \leq \theta \leq 60^\circ$ [Fig. 2(a)]; (b) same area after snowed in with new dry Snow of height $h_S \approx 0.31$ m, and compressed with snowshoes; (c) Brightness temperatures $T_B^{p,200^\circ}(\theta)$ measured for the three consecutive measurement scenarios "removed snow", "fresh dry snow", and "compressed snow".

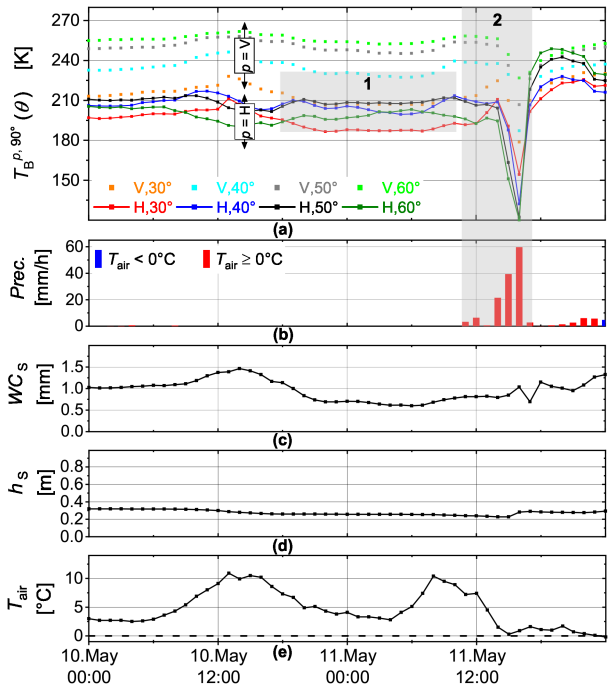

Fig. 13. Measured time-series for 10 May 2019 to 12 May 2019 during Campaign C3: (a) $T_B^{p,90^\circ}(\theta)$ for $\phi = 90^\circ$ ("natural area"); (b) Precipitation (*Prec.*); (c) Snow liquid Water-Column WC_S; (d) Snow height h_S; (e) air temperature T_{air}.

is questionable. This is because, depending on the temporal resolution and time of the observations, these methods may miss the response of T_B^p to short-term change cycles of WC_S. This is of utmost relevance when estimating the number of melt-days where it is possible to miss the signature to small amounts of liquid water content.

VIII. Snow Removal and Compression

In a field experiment in February 2015 performed at the Finnish Meteorological Institute's Arctic Research Center (FMI-ARC), snow was removed from the FP area of ELBARA-II to demonstrate for the first time the effect of dry snow on L-band brightness temperatures. The results, published in [56], corroborate the theoretical predictions of the LS-MEMLS developed in 2014 [22]. As shown in Fig. 12(a), we performed a similar experiment on 10 February 2017 during Campaign C1 in which dry snow cover was removed from ELBARA-IIs −9 dB FP areas corresponding to $\phi = 200^\circ$ and $35^\circ \leq \theta \leq 60^\circ$ [Fig. 2(a)]. As shown in the inset of Fig. 12(b), after a few weeks the FPs were covered with about 31 cm of fresh dry snow. Therefore, on 8 March 2017, we performed a snow compression experiment whereby we walked over the aforementioned FPs with snowshoes to mimic the situation of increased Snow density ρ_S. It is reiterated that as explained in Section V, snow compression is a relevant phenomenon. Hourly scans of FPs along $\phi = 200^\circ$ started before snow removal on 3 February 2017 at 10:00 and continued until the end of C1.

Fig. 12(c) shows the average $T_B^{p,200^\circ}(\theta)$ as functions of nadir angle θ, for p={H,V}, and the three consecutive measurement scenarios "removed snow", "fresh dry snow", and "compressed snow". It shows that $T_B^{H,200^\circ}(\theta)$ increases when the FP areas change from "removed snow" to "fresh dry snow", and finally to the "compressed snow" scenario. This increasing $T_B^{H,200^\circ}(\theta)$ with increasing ρ_S agrees with the LS-MEMLS simulations previously reported in [23]. It is known that the effect of changing dry Snow density ρ_S on $T_B^V(\theta)$ at vertical polarization is limited [23]. It is shown in [57] that near the Brewster angle, brightness temperatures at vertical polarization are least influenced by the snowpack. Strictly speaking, the definition of a Brewster angle ($\theta_{Brewster} = \arctan(n_2/n_1)$ where n_2 and n_1 are the refractive indices of the regions containing the incident and the transmitted wave) is only applicable to a double layer system (one interface). However, the cumulative Brewster effect of multiple dielectric interfaces leads to a Brewster-like angular behavior of emission at vertical polarization, meaning that emissivity at vertical polarization is maximal at a given observation angle. Accordingly, the difference between $T_B^{V,200^\circ}(\theta)$ for the "fresh dry snow" and the "compressed snow" scenarios is much smaller than the difference between "removed snow" and "fresh dry snow" scenarios. Accordingly, after the "removed snow" scenario $T_B^{V,200^\circ}(\theta)$ responds clearly to the formation of "fresh

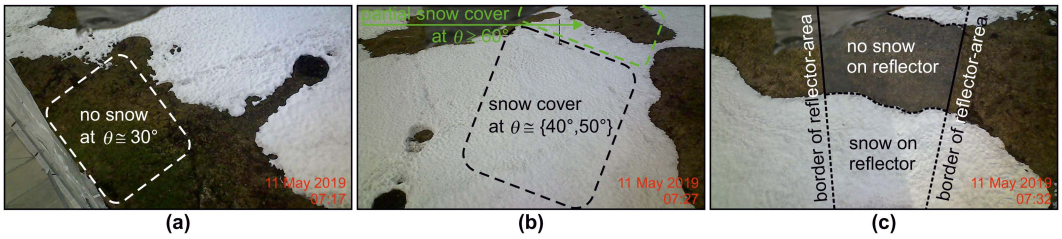

Fig. 14. Surveillance camera pictures taken during hourly RM scan on 11 May 2019. (a)–(c) Approximate RM view for three different azimuth angles $\phi = \{35^\circ, 90^\circ, 145^\circ\}$. These photos prove the existence of spatial snow cover heterogeneities at different nadir angles θ.

dry snow" with $\sim 20\,\mathrm{K}$ increase as is apparent in Fig. 12(c). Nevertheless, $T_\mathrm{B}^{\mathrm{V},200^\circ}(60^\circ)$ is $\sim 2.4\,\mathrm{K}$ larger for the "fresh dry snow" scenario with lower ρ_S than for the "compressed snow" scenario with correspondingly higher density. This is an experimental proof of the theoretical anticipation that for p=V and θ larger than the Brewster angle, $T_\mathrm{B}^p(\theta)$ decreases with increasing ρ_S of dry snow [23]. This effect is more distinguishable for snow cover over unfrozen ground.

IX. Spatial Heterogeneities

Emission model simulations such as performed with MEMLS [4] indicate that regardless of snow cover conditions, $T_\mathrm{B}^\mathrm{H}(\theta)$ should consistently decrease with increasing θ. However, when inspecting the time-series of $T_\mathrm{B}^p(\theta)$ in each campaign it is evident that the arrangement of $T_\mathrm{B}^p(\theta)$ for different nadir angles θ is sometimes mixed and thus appears to contradict theory. In some cases, this can be due to RFI contamination of measurements. However, even after rigorous RFI filtering, such examples exist in the brightness temperature time-series. Here, we use photographic records of the site to establish our hypothesis that such anomalous signatures can be due to the combined effect of 1) L-band RM scanning system and 2) existing spatial heterogeneities over the site. We first explain that, as illustrated in Fig. 2, in our L-band RM setups, elevation scanning across different θ means observing physically different FP areas. There can be conditions where different FP areas exhibit significantly different S-G SPs and thus influencing angular dependence of $T_\mathrm{B}^p(\theta)$. Fig. 13(a)–(e) presents the time-series of $T_\mathrm{B}^{p,90^\circ}(\theta)$ for $\phi = 90^\circ$ ("natural area"), Precipitation (*Prec.*), WC_S, h_S, and T_air, respectively, for 10 May 2019 to 12 May 2019 during Campaign C3. The shown brightness temperatures are filtered for non-thermal RFI. The gray rectangle 1 in Fig. 13(a) shows several hours with stable snow parameters and no precipitation where $T_\mathrm{B}^{\mathrm{H},90^\circ}(\theta)$ are misarranged with respect to θ. Fig. 14 shows three camera pictures taken during the same time. These pictures show that FP areas at $\theta = 30^\circ$ (close to the RM tower indicated in Fig. 2) and $\theta \geq 60^\circ$ (western and southwestern parts of the site) were snow-free. Accordingly, $T_\mathrm{B}^{\mathrm{H},90^\circ}(\theta)$ for $\theta = \{30^\circ, 60^\circ\}$ is smaller than for $\theta = \{40^\circ, 50^\circ\}$. As indicated with the gray rectangle 2 in Fig. 13, this time window is followed by a wet precipitation [Fig. 13(b)] over the site increasing the Snow liquid Water-Column WC_S [Fig. 13(c)] and soil moisture; this means decreasing the FP emissivity and $T_\mathrm{B}^{p,90^\circ}(\theta)$ at both polarization p={H,V}. Furthermore, the wet precipitation over the site temporarily decreases the FP spatial heterogeneities resulting in very similar values of $T_\mathrm{B}^{\mathrm{H},90^\circ}(\theta)$ for all θ.

X. Summary and Conclusion

This work presents an overview of an RS dataset from the Davos-Laret Remote Sensing Field Laboratory collected in an unprecedented effort for L-band radiometry of alpine snow cover during four consecutive winter Campaigns C1 (2016/2017), C2 (2017/2018), C3 (2018/2019), and C4 (2019/2020). In addition to the multiangle L-band Brightness temperatures $T_\mathrm{B}^{p,\phi}(\theta)$ measured at polarization p={H,V}, in-situ soil, snow, and meteorological measurements were collected whose summary was provided. The site schematics indicate that the measurements were designed to explore spatial heterogeneities over the site by scanning along various azimuth angles (ϕ) and at multiple nadir angles (θ). Furthermore, in-situ soil sensors, deployed along multiple transects, characterized the subnivean ground and its spatial heterogeneities. L-band radiometry was performed hourly to capture the effects of both short- and long-term events, such as precipitation and ground permittivity variations, respectively, on the upwelling microwave emission of the snow-covered ground.

Deployment of artificially created FootPrint (FP) areas was another key feature of the measurements at the Davos-Laret site. For example, the "charcoal-sand area" allowed for minimal surface scattering from the S-G interface and impedance matching to reduce the effect of the said interface on L-band emission. Furthermore, the "reflector area" (where a large metal-mesh was placed on the ground before snow accumulation) allowed for the exclusive measurement of L-band emission of snow, which is in direct relationship with the Snow liquid Water-content W_S. Accordingly, Snow liquid Water-Column WC_S, estimated from $T_\mathrm{R}^p(\theta)$ over exclusively the "reflector area" and measured Snow height h_S, was used as a "derived measurement" to study the response of $T_\mathrm{B}^{p,\phi}(\theta)$ to S-G SPs and meteorological events such as dry and wet precipitations.

Four key data analysis examples were provided to experimentally investigate the theoretically anticipated response of $T_\mathrm{B}^{p,\phi}(\theta)$ to S-G state variations. In some cases, experimental "long-term" proofs were missing. Accordingly, examples were provided and discussed where the effect of wet and dry precipitation on $T_\mathrm{B}^{p,\phi}(\theta)$ is evident. It was shown that $T_\mathrm{B}^{p,\phi}(\theta)$, especially at polarization p=H, temporarily increases in response to the lower density snow layer formed atop the snowpack as a result of

intense dry snowfall that strengthens impedance match between air and the snowpack. Thanks to the long time-series of measurements stretched over several years, multiple instances of each of the studied phenomena can be found, hence the "long-term" proofs.

The overview of all measurements (Section V), the effect of spatial heterogeneities on the angular pattern of $T_{\mathrm{B}}^{p,\phi}(\theta)$ (Section IX), and the overview of all campaigns' RM data as a function of θ and in the framework of snow cover state (Section VI) are examples on how this dataset can be inspected, visualized, or used in future scientific analysis. Accordingly, the data presented are made available in [30].

A general finding that can be derived from the L-band $T_{\mathrm{B}}^{p}(\theta)$ time-series measured during the four campaigns is the following: In contrast to passive microwave measurements at higher frequencies, it is rare at L-band that the emission of a seasonal snowpack behaves like a "black body" ($T_{\mathrm{B}}^{p}(\theta) \leq 273.15\,\mathrm{K}$ at any θ). In our observations, "black body"-like emission was most likely observed for the largest θ during the "isothermal" phases in C1, C2, and C3; for the "isothermal" phase in C4, this was not the case. It seems that "black body"-like emission at L-band is most likely when the snowpack is sufficiently moist to shield emission from the ground, but moisture in the top layer of the snowpack is not too high to dominate $T_{\mathrm{B}}^{p}(\theta)$ via the high reflectivity of the snow–air interface.

In summary, in addition to a comprehensive RS dataset, made available in [30], this work provides novelties such as 1) using WC_{S} as "derived measurements" for in-depth analysis of $T_{\mathrm{B}}^{p,\phi}(\theta)$, 2) artificial FPs such as the "reflector area" and the "charcoal-sand area", and 3) snowpack manipulations (compression and removal). Furthermore, the four consecutive campaigns offer several key take-away messages for future work and similar efforts. First, it is important to maintain a temporal resolution suitable for capturing the phenomena of interest. For example, intense snow precipitation changes SWE and Snow density ρ_{S}; however, its observed effect on $T_{\mathrm{B}}^{p,\phi}(\theta)$ depends on the temporal resolution of radiometry. Second, when performing scientific campaigns, video and photographic documentation of the environment is critically helpful in providing detailed insight into the changes in the environment and the snowpack. For instance, pictures easily highlight the relevance of snow surface topography and preferential meltwater flow paths. Third, it is important to establish long-term measurements to develop a large enough umbrella of knowledge covering multiple key phenomena, which influence scattering and microwave emission of the S-G system. These long-term measurements should consist of a baseline of measurements, which in our case was L-band radiometry over "natural area" and "reflector area" as well as auxiliary soil, snow, and meteorological measurements. Additional components and modifications can be introduced depending on the targeted scientific questions. For example, the creation of the "charcoal-sand area" and the introduction of additional in-situ sensor transects were further components introduced in Campaigns C2 and C4.

Finally, it is prudent to use the presented dataset in the future to understand and improve the performance of Snow density and Ground permittivity $(\rho_{\mathrm{S}}, \epsilon_{\mathrm{G}})$ retrieved from L-band RM data with the approach first proposed in [23], analyzed theoretically in [55], further developed and applied to close-range brightness temperatures in [28] and [56], and used for the first time with satellite-based $T_{\mathrm{B}}^{p}(\theta)$ in [24]. It will allow to draw conclusions on the retrieval performances in various conditions such as frozen/unfrozen ground and in the presence of moisture (liquid water) in the snowpack.

ACKNOWLEDGMENT

The authors would like to appreciate the support of the company "Kessler Betriebe AG" for their help in each campaign with the logistics and installation of the RM on the tower. Furthermore, the authors appreciate the support from their colleagues at the Swiss Federal Research Institute for Snow, Forest, and Landscape research (WSL) for all their support, including Manfred Stähli, Henning Löwe, and Matthias Jaggi.

REFERENCES

[1] W. H. Stiles and F. T. Ulaby, "The active and passive microwave response to snow parameters: 1. Wetness," *J. Geophys. Res.: Oceans*, vol. 85, no. C2, pp. 1037–1044, 1980.

[2] F. T. Ulaby and W. H. Stiles, "The active and passive microwave response to snow parameters: 2. Water equivalent of dry snow," *J. Geophys. Res.: Oceans*, vol. 85, no. C2, pp. 1045–1049, 1980.

[3] T. Weise and C. Matzler, "Radiometric and structural measurements of snow samples," in *Proc. Geosci. Remote Sens. Symp., Int. Quantitative Remote Sens. Sci. Appl.*, 1995, vol. 3, pp. 1762–1764.

[4] A. Wiesmann and C. Mätzler, "Microwave emission model of layered snowpacks," *Remote Sens. Environ.*, vol. 70, no. 3, pp. 307–316, 1999.

[5] C. Mätzler, H. Aebischer, and E. Schanda, "Microwave dielectric properties of surface snow," *IEEE J. Ocean. Eng.*, vol. JOE-9, no. 5, pp. 366–371, Dec. 1984.

[6] R. Hofer and W. Good, "Snow parameter determination by multichannel microwave radiometry," *Remote Sens. Environ.*, vol. 8, no. 3, pp. 211–224, 1979.

[7] W. E. Nichols, R. H. Cuenca, T. J. Schmugge, and J. R. Wang, "Pushbroom microwave radiometer results from HAPEX-MOBILHY," *Remote Sens. Environ.*, vol. 46, no. 2, pp. 119–128, 1993.

[8] C. T. Swift, D. M. LeVine, and C. S. Ruf, "Aperture synthesis concepts in microwave remote sensing of the earth," *IEEE Trans. Microw. Theory Techn.*, vol. 39, no. 12, pp. 1931–1935, Dec. 1991.

[9] J. Galantowicz and A. England, "Radiobrightness signatures of energy balance processes: Melt/freeze cycles in snow and prairie grass covered ground," in *Proc. IEEE Int. Geosci. Remote Sens. Symp.*, 1994, vol. 1, pp. 596–598.

[10] A. England and J. Galantowicz, "A volume emission model for the radiobrightness of prairie grass," in *Proc. IEEE Int. Geosci. Remote Sens. Symp.*, 1994, vol. 4, pp. 2463–2465.

[11] E. Kim and A. England, "Passive microwave freeze/thaw classification for wet tundra regions," in *Proc. Int. Geosci. Remote Sens. Symp.*, 1996, vol. 4, pp. 2267–2269.

[12] Y.-A. Liou, E. Kim, and A. England, "Radiobrightness of prairie soil and grassland during dry-down simulations," *Radio Sci.*, vol. 33, no. 2, pp. 259–265, 1998.

[13] J. Judge et al., "A growing season land surface process/radiobrightness model for wheat-stubble in the Southern Great Plains," *IEEE Trans. Geosci. Remote Sens.*, vol. 37, no. 5, pp. 2152–2158, Sep. 1999.

[14] A. England and R. DeRoo, "Active layer thickness and moisture content of arctic tundra from SVAT/Radiobrightness models and assimilated 1.4 or 6.9 GHz brightness," Final Rep. NSF Award ID 240747, 2006.

[15] B. K. Hornbuckle, A. W. England, R. D. De Roo, M. A. Fischman, and D. L. Boprie, "Vegetation canopy anisotropy at 1.4 GHz," *IEEE Trans. Geosci. Remote Sens.*, vol. 41, no. 10, pp. 2211–2223, Oct. 2003.

[16] F. T. Ulaby, R. K. Moore, and A. K. Fung, *Microwave Remote Sensing: Active and Passive. Volume 1—Microwave Remote Sensing Fundamentals and Radiometry*. Reading, MA, USA: Addison Wesley, 1981.

[17] F. T. Ulaby, R. K. Moore, and A. K. Fung, *Microwave Remote Sensing Active and Passive. Radar Remote Sensing and Surface Scattering and Emission Theory*. Reading, MA, USA: Addison Wesley, 1982.
[18] F. Ulaby, R. Moore, and A. Fung, *Microwave Remote Sensing: Active and Passive, From Theory to Applications*. Norwood, MA, USA: Artech House, 1986.
[19] Y. H. Kerr et al., "The SMOS mission: New tool for monitoring key elements of the global water cycle," *Proc. IEEE*, vol. 98, no. 5, pp. 666–687, May 2010.
[20] D. Entekhabi et al., "The Soil Moisture Active Passive (SMAP) mission," *Proc. IEEE*, vol. 98, no. 5, pp. 704–716, May 2010.
[21] R. Hofer and C. Mätzler, "Investigations on snow parameters by radiometry in the 3- to 60-mm wavelength region," *J. Geophys. Res.: Oceans*, vol. 85, no. C1, pp. 453–460, 1980.
[22] M. Schwank et al., "Model for microwave emission of a snow-covered ground with focus on L band," *Remote Sens. Environ.*, vol. 154, pp. 180–191, 2014.
[23] M. Schwank et al., "Snow density and ground permittivity retrieved from L-band radiometry: A synthetic analysis," *IEEE J. Sel. Topics Appl. Earth Observ. Remote Sens.*, vol. 8, no. 8, pp. 3833–3845, Aug. 2015.
[24] J. Lemmetyinen et al., "Retrieval of snow parameters from L-band observations-application for SMOS and SMAP," in *Proc. IEEE Int. Geosci. Remote Sens. Symp.*, 2016, pp. 7067–7070.
[25] Z. Su et al., "Multiyear in-situ L-band microwave radiometry of land surface processes on the Tibetan Plateau," *Sci. Data*, vol. 7, no. 1, pp. 1–13, 2020.
[26] Ł. Gluba et al., "Spatio-temporal mapping of L-band microwave emission on a heterogeneous area with ELBARA III passive radiometer," *Sensors*, vol. 19, no. 16, 2019, Art. no. 3447.
[27] R. Naderpour, M. Schwank, and C. Mätzler, "Davos–Laret Remote Sensing Field Laboratory: 2016/2017 winter season L-band measurements data-processing and analysis," *Remote Sens.*, vol. 9, no. 11, 2017, Art. no. 1185.
[28] M. Schwank and R. Naderpour, "Snow density and ground permittivity retrieved from L-band radiometry: Melting effects," *Remote Sens.*, vol. 10, no. 2, 2018, Art. no. 354.
[29] R. Naderpour and M. Schwank, "Snow wetness retrieved from L-band radiometry," *Remote Sens.*, vol. 10, no. 3, 2018, Art. no. 359.
[30] R. Naderpour, M. Schwank, D. Houtz, and C. Mätzler, "L-band radiometry of alpine seasonal snow cover: 4 years at the Davos-Laret Remote Sensing Field Laboratory," 2022. [Online]. Available: https://www.envidat.ch/dataset/l-band-davos-laret
[31] R. Naderpour, D. Houtz, and M. Schwank, "Snow wetness retrieved from close-range L-band radiometry in the western Greenland ablation zone," *J. Glaciol.*, vol. 67, no. 261, pp. 27–38, 2020.
[32] D. Houtz, R. Naderpour, and M. Schwank, "Retrievals of snow properties over Greenland from L-band radiometry," in *Proc. IEEE Int. Geosci. Remote Sens. Symp.*, 2019, pp. 3990–3993.
[33] D. Houtz, C. Mätzler, R. Naderpour, M. Schwank, and K. Steffen, "Quantifying surface melt and liquid water on the Greenland ice sheet using L-band radiometry," *Remote Sens. Environ.*, vol. 256, 2021, Art. no. 112341.
[34] H. M. Pickett, J. C. Hardy, and J. Farhoomand, "Characterization of a dual-mode horn for submillimeter wavelengths (short papers)," *IEEE Trans. Microw. Theory Techn.*, vol. TMTT-32, no. 8, pp. 936–937, Aug. 1984.
[35] C. L. Werner et al., "Processing and calibration of continuous snowpack measurements using the WBSCAT polarimetric microwave scatterometer during winter 2018–2019 at Davos Switzerland," in *Proc. AGU Fall Meeting Abstr.*, 2019, vol. 2019, Paper C33E–1639.
[36] C. Werner, O. Frey, R. Naderpour, A. Wiesmann, M. Süss, and U. Wegmüller, "Aperture synthesis and calibration of the WBSCAT ground-based scatterometer," in *Proc. IEEE Int. Geosci. Remote Sens. Symp.*, 2021, pp. 1947–1949.
[37] C. Werner, M. Suess, U. Wegmüller, O. Frey, and A. Wiesmann, "The ESA wideband microwave scatterometer (Wbscat): Design and implementation," in *Proc. IEEE Int. Geosci. Remote Sens. Symp.*, 2019, pp. 8339–8342.
[38] R. Naderpour, M. Schwank, D. Houtz, C. Werner, and C. Mätzler, "Wideband backscattering from alpine snow cover: A full-season study," *IEEE Trans. Geosci. Remote Sens.*, vol. 60, 2022, Art. no. 4302215.
[39] C. Werner, A. Wiesmann, T. Strozzi, M. Schneebeli, and C. Mätzler, "The SnowScat ground-based polarimetric scatterometer: Calibration and initial measurements from Davos Switzerland," in *Proc. IEEE Int. Geosci. Remote Sens. Symp.*, 2010, pp. 2363–2366.
[40] C. Werner, O. Frey, U. Wegmüller, A. Wiesmann, and M. Suess, "The WBSCAT polarimetric synthetic aperture scatterometer for retrieval of in-situ time-series of snow structure," in *Proc. AGU Fall Meeting Abstr.*, 2018, vol. 2018, Paper C13D–1172.
[41] M. Schwank et al., "ELBARA II, an L-band radiometer system for soil moisture research," *Sensors*, vol. 10, no. 1, pp. 584–612, 2010.
[42] T. Pellarin et al., "Two-year global simulation of L-band brightness temperatures over land," *IEEE Trans. Geosci. Remote Sens.*, vol. 41, no. 9, pp. 2135–2139, Sep. 2003.
[43] M. Schwank, E. Lopez-Baeza, J.-P. Wigneron, I. Völksch, C. Mätzler, and Y. Kerr, "L-band radiative properties of vine vegetation at the SMOS cal/val site MELBEX III," in *Proc. 39th COSPAR Sci. Assem.*, 2012, vol. 39, Paper 1742.
[44] M. Dimitrov et al., "New improved algorithm for sky calibration of L-band radiometers JÜLBARA and ELBARA-II," in *Proc. 12th Specialist Meeting Microw. Radiometry Remote Sens. Environ.*, 2012, pp. 1–4.
[45] C. Mätzler et al., "ELBARA, the ETH L-band radiometer for soil-moisture research," in *Proc. IEEE Int. Geosci. Remote Sens. Symp.*, 2003, vol. 5, pp. 3058–3060.
[46] K. Schneeberger, M. Schwank, C. Stamm, P. De Rosnay, C. Matzler, and H. Fluhler, "Topsoil structure influencing soil water retrieval by microwave radiometry," *Vadose Zone J.*, vol. 3, no. 4, pp. 1169–1179, 2004.
[47] M. Schwank, C. Matzler, M. Guglielmetti, and H. Fluhler, "L-band radiometer measurements of soil water under growing clover grass," *IEEE Trans. Geosci. Remote Sens.*, vol. 43, no. 10, pp. 2225–2237, Oct. 2005.
[48] I. Völksch, M. Schwank, and C. Mätzler, "L-band reflectivity of a wire grid above a dielectric surface," *IEEE Geosci. Remote Sens. Lett.*, vol. 7, no. 3, pp. 601–605, Jul. 2010.
[49] M. Schwank, M. Guglielmetti, C. Mätzler, and H. Flühler, "Testing a new model for the L-band radiation of moist leaf litter," *IEEE Trans. Geosci. Remote Sens.*, vol. 46, no. 7, pp. 1982–1994, Jul. 2008.
[50] R. D. De Roo, S. Misra, and C. S. Ruf, "Sensitivity of the kurtosis statistic as a detector of pulsed sinusoidal RFI," *IEEE Trans. Geosci. Remote Sens.*, vol. 45, no. 7, pp. 1938–1946, Jul. 2007.
[51] H. R. Bogena, J. A. Huisman, B. Schilling, A. Weuthen, and H. Vereecken, "Effective calibration of low-cost soil water content sensors," *Sensors*, vol. 17, no. 1, 2017, Art. no. 208.
[52] J.-K. Son, W.-T. Shin, and J.-Y. Cho, "Laboratory and field assessment of the decagon 5TE and GS3 sensors for estimating soil water content in saline-alkali reclaimed soils," *Commun. Soil Sci. Plant Anal.*, vol. 48, no. 19, pp. 2268–2279, 2017.
[53] J. L. Varble and J. Chávez, "Performance evaluation and calibration of soil water content and potential sensors for agricultural soils in eastern colorado," *Agricultural Water Manage.*, vol. 101, no. 1, pp. 93–106, 2011.
[54] M. Guglielmetti, M. Schwank, C. Matzler, C. Oberdorster, J. Vanderborght, and H. Flühler, "FOSMEX: Forest soil moisture experiments with microwave radiometry," *IEEE Trans. Geosci. Remote Sens.*, vol. 46, no. 3, pp. 727–735, Mar. 2008.
[55] R. Naderpour, M. Schwank, C. Mätzler, J. Lemmetyinen, and K. Steffen, "Snow density and ground permittivity retrieved from L-band radiometry: A retrieval sensitivity analysis," *IEEE J. Sel. Topics Appl. Earth Observ. Remote Sens.*, vol. 10, no. 7, pp. 3148–3161, Jul. 2017.
[56] J. Lemmetyinen et al., "Snow density and ground permittivity retrieved from L-band radiometry: Application to experimental data," *Remote Sens. Environ.*, vol. 180, pp. 377–391, 2016.
[57] C. Mätzler, "Applications of SMOS over terrestrial ice and snow," in *Proc. 3rd SMOS Workshop*, 2001, pp. 10–12.

Reza Naderpour received the M.Sc. degree in radio science and engineering from Aalto University, Espoo, Finland, in 2014, and the D.Sc. degree in environmental systems science from ETH Zürich, Zürich, Switzerland, in 2019.

During his time with Aalto University, he conducted research on a wide range of topics including radio wave propagation and channel modeling for 5G network R&D and space weather. He has participated in two scientific expeditions over the Greenland ice sheet and in the MOSAiC expedition in central Arctic Ocean. His main research interests include microwave remote sensing of cryosphere, monitoring glacial, and sea ice dynamics, also working on developing low-cost field-capable microwave instruments for measuring dielectric properties of natural media.

Dr. Naderpour received the Silver Medal of ETH Zürich for distinguished doctoral theses in 2020.

Mike Schwank was born in Zürich, Switzerland, in 1966. He received the bachelor's degree in electrical engineering and the Ph.D. degree in physics from ETH Zürich, Zürich, in 1989 and 1999, respectively.

He has part-time employments with Gamma Remote Sensing Research and Consulting, Ltd., Gümligen, Switzerland, from 2007 to 2009 and since 2013, and the Swiss Federal Research Institute WSL, Birmensdorf, Switzerland. He is experienced with industrial research and development in the fields of micro-optics and telecommunications from 1999 to 2003. He is also experienced with leading Ph.D. students and the coordination of large research projects, such as Terrestrial Environmental Observatories (TERENO). His current research interest includes microwave remote sensing studies in support of Soil Moisture and Ocean Salinity and future satellite missions.

Derek Houtz was born in Washington, DC, USA, in 1989. He received the Ph.D. degree in aerospace engineering from the University of Colorado (Boulder) with specializing in microwave remote sensing and radiometer calibration in 2017.

He has been engaged in environmental monitoring for over a decade. He has been bringing strong skills in hardware and software development, microwave radiometry, and field research implementation. With research assistant and postdoctoral positions with the National Institute of Standards and Technology (NIST), he developed traceable radiometer calibration sources. In parallel, he was a Field Assistant and Data Analyst for the Greenland Climate Network (GC-Net) for the Cooperative Institute for Research in Environmental Studies (CIRES), Boulder, CO, from 2013 to 2018. Joining the Swiss Federal Institute for Forest, Snow and Landscape Research (WSL) in 2018, he has contributed to active and passive microwave remote sensing research for algorithm development, field campaigns, and hardware. In 2020, he founded TerraRad Tech AG, Zürich, Switzerland. He built the first TerraRad Tech L-band radiometer prototypes in the lab with WSL, and applied for a European patent in 2020 based on a highly efficient L-band antenna.

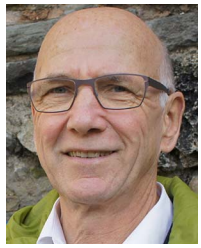

Christian Mätzler received the M.Sc. degree in physics, with minors in mathematics and geography, and the Ph.D. degree in physics, with minors in solar radio astronomy, from the University of Bern, Bern, Switzerland, in 1970 and 1974, respectively.

After the postdoctoral research with NASA Goddard Space Flight Center, Greenbelt, MD, and with the Swiss Federal Institute of Technology (ETH), Zürich, Switzerland, he became a Research Group Leader for terrestrial and atmospheric radiometry and remote sensing with the Institute of Applied Physics, University of Bern, in 1978. He got the habilitation in applied physics in 1986 and the title of a Titular Professor in 1992. His teaching included principles of remote sensing, imaging radiometry, radar meteorology, and radiative transfer. After retirement in July 2010, he started as a consultant for Gamma Remote Sensing, Gümligen, Switzerland. His studies have concentrated on microwave (1–100 GHz) signatures for active and passive remote sensing of the atmosphere, snow, ice, soil, and vegetation, as well as on the development of methods for dielectric and propagation measurements for such media. He is the Editor of a book on thermal microwave emission with applications for remote sensing. Furthermore, he has been interested in special ice forms, such as hair ice.